# Using simplified methods to explore the impact of parameter uncertainty on CO2 storage estimates with application to the Norwegian Continental Shelff

Rebecca Allen, Halvor M. Nilsen, Knut-Andreas Lie, Olav Møyner, Odd Andersen

Citation:
Rebecca Allen, Halvor M. Nilsen, Knut-Andreas Lie, Olav Møyner, Odd Andersen (2018) Using simplified methods to explore the impact of parameter uncertainty on CO2 storage estimates with application to the Norwegian Continental Shelff. International Journal of Greenhouse Gas Control Vol. 75, August 2018, Pages 198-213 DOI: https://doi.org/10.1016/j.ijggc.2018.05.017

# Using Simplified Methods to Explore the Impact of Parameter Uncertainty on $CO_2$ Storage Estimates with Application to the Norwegian Continental Shelf

Rebecca Allen[a,*], Halvor M. Nilsen[a], Knut-Andreas Lie[a], Olav Møyner[a], Odd Andersen[a]

[a]*SINTEF Digital, Mathematics and Cybernetics, PB 124 Blindern, 0314 Oslo, Norway*

**Abstract**

We use simplified methods to investigate how uncertainty in geological models affects practical $CO_2$ storage capacities in large-scale saline aquifers. Our focus is on uncertainties in top-surface elevation, rock properties (porosity, permeability), fault transmissibility, and aquifer conditions (pressure and temperature). To quantify the statistical characteristics of static trapping capacity and dynamic estimates of plume migration, we create hundreds of possible realizations of the geomodel by applying Gaussian-type perturbations to the spatially correlated properties. Two different simplified methods are introduced to reduce the computational cost of simulating migration over thousands of years in all the model realizations, which each spans hundreds of kilometers. First, we use vertical-equilibrium (VE) modelling, which is orders of magnitude faster than solving the 3D flow equations. Second, we introduce a fast look-ahead algorithm that enables us to exit the VE simulation once a pseudo-steady state is reached. This algorithm uses a spill-point analysis of the top-surface's trapping structure to forecast how much $CO_2$ will eventually become trapped and how much will leak through open boundaries of the formation. This reduces the computational cost significantly, since we seldom need to simulate long-term migration past a few hundred or thousand years.

*Keywords:* $CO_2$ storage, Sensitivity analysis, Parameter uncertainty, Spill-point analysis, Vertical-equilibrium simulation, Migration forecast

## 1. Introduction

Geological storage of carbon dioxide is viewed as a promising and necessary strategy to combat climate change. Estimating the static and dynamic storage capacity is an important step when ranking or selecting aquifers as potential storage sites. Simple volumetric calculations are sufficient to bound the available pore space (static capacity). To obtain more realistic bounds on the actual storage volume that can be achieved in a practical storage operation (dynamic capacity) one also needs flow simulations of specific or representative storage scenarios. Injectivity and pressure build-up will in many cases be the main limiting factors, but for dipping, open aquifers containing relatively few structural closures, the practical capacity of certain storage sites could equally well be bounded by the long-term migration of the $CO_2$ plume (Chadwick et al., 2008). Estimating pressure buildup and the extent of plume migration in the aquifer is therefore crucial when evaluating which storage strategy poses the least amount of risk (preserves caprock integrity, minimizes $CO_2$ leakage, avoids ground water contamination, etc). Long-term migration can either be simulated by standard flow equations, or forecast using the trapping structure of the formation's top-surface obtained from a spill-point analysis.

To provide value in decision making, estimates of both storage capacity and plume dynamics need to account for the significant uncertainty inherent in geomodel parameters. Standard methods to quantify this uncertainty rely on considering many possible realizations of the geomodel (known as a statistical ensemble), and quantifying the statistical measures of the ensemble such as mean and standard deviation (Bear and Cheng, 2010). Estimating static/volumetric capacity is computationally inexpensive, and can be performed for a large ensemble without difficulty. On the other hand, performing highly resolved simulations on all members of a large model ensemble can quickly become computationally intractable. Solutions to this problem include either reducing the number of ensemble members, or speeding up the simulations required for each geomodel realization.

Previous work has examined how parameter uncertainty influences $CO_2$ storage modelling. A wide range of parameters that control geological heterogeneities have been considered, such as porosity (Manceau and Rohmer,

*Corresponding author.

*Email addresses:* Rebecca.Allen@sintef.no (Rebecca Allen), HalvorMoll.Nilsen@sintef.no (Halvor M. Nilsen), KnutAndreas.Lie@sintef.no (Knut-Andreas Lie), Olav.Moyner@sintef.no (Olav Møyner), Odd.Andersen@sintef.no (Odd Andersen)

2014; Han et al., 2011; Sarkarfarshi et al., 2014), permeability (either absolute, relative, anisotropy) (Manceau and Rohmer, 2014; Han et al., 2011; Sarkarfarshi et al., 2014; Lothe et al., 2016), seal permeability (Birkholzer et al., 2009), presence of faults and their transmissibility (Birkholzer et al., 2011; Lothe et al., 2014, 2016; Ashraf et al., 2013), ratio of sand to shale content (Flett et al., 2007), and top-surface morphology (Nilsen et al., 2012; Shariatipour et al., 2016; Goater et al., 2013; Gasda et al., 2012, 2013). Other parameters considered include pore compressibility (Birkholzer et al., 2009), capillary pressure (Manceau and Rohmer, 2014; Sarkarfarshi et al., 2014), and the residual saturations and densities of $CO_2$ and brine (Han et al., 2011; Sarkarfarshi et al., 2014). Variability has been represented stochastically, or treated in a homogeneous sense by testing only $N$ homogeneous permeability values, for example. Broadly speaking, studies have assessed parameter sensitivity on trapping mechanisms, plume migration, and risk of leakage. More specifically, studies have measured model responses such as moment of inertia of the $CO_2$ plume (Sarkarfarshi et al., 2014); pressure (Ashraf et al., 2013; Birkholzer et al., 2009); boundary fluxes (Ashraf et al., 2010); mass of $CO_2$ in mobile, residual, or other phases (Ashraf et al., 2013; Han et al., 2011; Flett et al., 2007); distance of upslope $CO_2$ plume migration (Manceau and Rohmer, 2014; Gasda et al., 2012, 2013); connected $CO_2$ volumes (Ashraf et al., 2010); and structural trapping volumes (Nilsen et al., 2012; Gasda et al., 2013). Various geomodels have been used, including synthetic models intended to represent realistic storage sites (e.g., a 2D box model (Han et al., 2011), a stratified model (Birkholzer et al., 2009), multiple plausible realizations of shallow-marine reservoirs (Ashraf et al., 2010), a dipping box model with a surface topography containing buried beach or offshore sand ridges combined with four different fault patterns (Nilsen et al., 2012)), as well as models of real sandstone formations (e.g., the Paris basin in France (Manceau and Rohmer, 2014), the Southern San Joaquin Valley in California, USA (Birkholzer et al., 2011)).

The outcome of the studies listed above is not always definitive in determining which parameters influence model response the most for a few reasons. First, the characteristics of $CO_2$ storage can vary significantly from site to site. Second, some of the models considered are hypothetical or synthetic versions of real aquifers. Third, only a selection of uncertain parameters is usually evaluated, not an exhaustive list, thus the "most influential" parameter on the model response is only relative to those considered. Indeed, in most of these studies, the main point has been to develop general methods for ranking the importance of uncertain parameters and not providing specific rankings; e.g., Manceau and Rohmer (2016); Sarkarfarshi et al. (2014).

The main objective of our study is to present computational methods for examining how selected model parameters influence structural trapping capacity and plume migration in large-scale aquifers systems of the types seen on the Norwegian Continental Shelf. In doing so, we demonstrate how the use of simplified methods, namely vertical-equilibrium modelling and migration forecasting, can make sensitivity analysis studies more computationally tractable. The focus of this work is not about providing a robust uncertainty analysis, however based on our observations we analyze and discuss how each parameter influences storage capacity estimates. The parameters we focus on are heterogeneous rock properties, top-surface elevations, initial conditions, and fault transmissibilities. These parameters are considered to be a good starting point for a thorough sensitivity analysis because they are highly uncertain in large-scale aquifers, for which data are generally scarce. Of course, many other parameters could be investigated, but our objective is not an exhaustive sensitivity study. Given this limitation, we will not definitively conclude which parameters are most influential in $CO_2$ storage modelling, rather we will only state the impact observed in the particular cases we consider. To illustrate the methods in a semi-realistic setting, we apply them to models of top-seal topologies derived from public data of real aquifers, possibly accompanied by representative petrophysical properties of the underlying sands, taken from the $CO_2$ Storage Atlas of the Norwegian Continental Shelf (Halland et al., 2014). We emphasize that any actual storage capacity estimates we present should not be interpreted literally as being representative of named aquifers. Many of the parameters and uncertainty ranges entering our model simulations are pure guesstimates and need to be replaced by site-specific and quality-assured numbers. However, once this is done, we believe the methodology can be used to explore the impact of parameter uncertainty on storage capacity estimates.

## 2. Method

In this section, we first explain how we have chosen to represent parameter uncertainty or variability in our geomodels. We present the similarity index used to quantify the difference between plume migration simulated with a base geomodel and perturbed versions thereof. We also explain how structural trapping capacity is computed based on geometrical trap volumes, porosity, and $CO_2$ density at aquifer conditions and thereafter briefly outline vertical-equilibrium modelling and our new migration forecast method.

### *2.1. Representing parameter uncertainty*

To assess how uncertainty in the topography of the caprock and the porosity and permeability of the aquifer impacts storage capacity estimation and long-term plume migration, we start from a base model and perturb

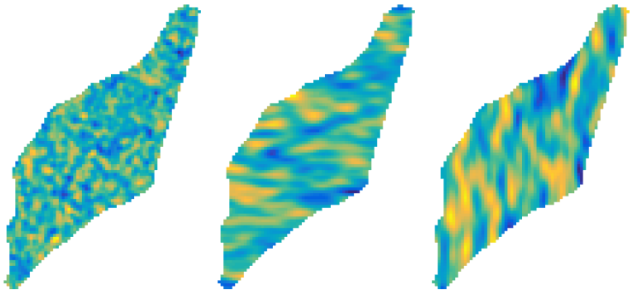

Figure 1: Various Gaussian-type perturbations that could be scaled and applied to top-surface elevations, porosity, and permeability. Blue to yellow colors represent the range of values between a specified minimum and maximum.

these parameters one at a time by adding an approximate Gaussian random field. For each parameter, one hundred realizations are used to form an ensemble. Figure 1 shows example Gaussian fields with different spatial correlations. Caprock elevations are perturbed using a field similar to the first plot, while porosity and permeability are perturbed using anisotropic fields similar to the second and third plots. Various interval extremes of these fields are tested and are reported with the results. These perturbations are arbitrary and intended to be illustrative rather than representative of actual uncertainty ranges. For simplicity, the perturbations were generated on the rectangular bounding box of the aquifer, and hence the extremal values of the perturbed fields will not necessarily coincide with the prescribed min and max values when the aquifer does not completely fill its bounding box. However, in our results section, we state the original min/max values used to generate the perturbation fields rather than the actual extremal values since the difference is small.

Uncertainty in the aquifer temperature and pressure are also important to consider since these affect the $CO_2$ density, which further impacts estimates of plume migration and storage capacity. For example, a publicly-released geomodel of the Sleipner storage site initially came with a list of parameters that suggested a $CO_2$ density of 760 kg/m$^3$, presumably based on an aquifer temperature calculated using a thermal gradient of 35.6°C/km (Singh et al., 2010). However, recent studies have explored the possibility of a warmer aquifer that results in a lower $CO_2$ density (Cavanagh and Nazarian, 2014; Cavanagh et al., 2015), which in turn opens the possibility of obtaining a better match between seismic observations and the simulated plume outline (Nilsen et al., 2017). Herein, the sensitivity of the capacity estimate to initial aquifer conditions is assessed by altering the thermal gradient used to compute caprock temperature, and deviating the initial hydrostatic pressure $P$ by a specific percentage of the mean hydrostatic pressure in the aquifer. More specifically, initial caprock pressure $P_0$ is computed by

$$P = (\rho_w g z + P_s)\,, \tag{1}$$

$$P_0 = P + \frac{\sum_i^n (pv_i P_i)}{\sum_i^n pv_i} d/100, \tag{2}$$

where $\rho_w$ is water density, $g$ gravitational acceleration, $z$ caprock depth, $P_s$ surface pressure, $pv_i$ pore volume of cell $i$, and $d$ the deviation in percent. Equation (1) is caprock pressure assuming hydrostatic conditions. In the second term on the right hand side of (2), $d$ is being multiplied with the pore-volume weighted average of the caprock pressure. In this work, we assume a water density of 1020 kg/m$^3$, and a surface pressure of one atmosphere. For initial caprock temperature $T$, a linear relationship between seafloor temperature $T_\mathrm{b}$ and depth below seafloor $(z - z_\mathrm{b})$ is assumed, i.e.,

$$T = T_\mathrm{b} + \nabla T\,(z - z_\mathrm{b})\,, \tag{3}$$

where $\nabla T$ is the thermal gradient in the vertical direction. For the North Sea formations we consider herein, we assume a seafloor depth of 100 meters, a seafloor temperature of 7°C, and a thermal gradient of 35.6°C/km. These values are similar to those used in the Sleipner benchmark model (Singh et al., 2010). All of the aforementioned values are uncertain, and hence we investigate the impact of assuming warmer or cooler geomodels simply by varying the thermal gradient. In our simulations, the aquifer temperature is assumed to remain constant (i.e., an isothermal model).

### *2.2. Quantifying impact on flow and migration*

Previous literature suggests a few different ways to quantify the discrepancy in plume migration between two different geomodel realizations. One approach is to compute the center of mass for each plume at a given

point in time, and then compare these locations relative to a point of reference (e.g., the center of mass in a base case, or the injection point); see e.g., Manceau and Rohmer (2014, 2016); Han et al. (2011). Another approach is to compute the Sørensen–Dice coefficient,

$$S = \frac{2C}{A + B}, \tag{4}$$

which was originally formulated to quantify the coincidence of two different species found in nature (Dice, 1945), but has recently been used as a similarity index to compare simulated and observed $CO_2$ footprints at the Ketzin storage site (Lüth et al., 2015). For our purposes, $A$ and $B$ are the plume footprints produced by two different geomodels (e.g., the base case and a perturbed case), and $C$ is the overlapping footprint. If two geomodels produce identical plume footprints, the coefficient $S$ is equal to unity. As the discrepancy between plumes $A$ and $B$ becomes larger (or the footprint overlap becomes smaller), $S$ tends to zero. The disadvantage of the above two approaches is that they do not capture the degree of similarity between two migration pathways, rather they only reflect the similarity of the plume position at a given instance in time. Nonetheless, (4) provides us with a simple way to quantify the similarity between simulated $CO_2$ plumes in two different geomodels.

### *2.3. Geomodels*

The geomodels we consider in this work are publicly available from the Norwegian Petroleum Directorate (NPD), as part of their $CO_2$ Storage Atlas of the Norwegian Continental Shelf (Halland et al., 2014). Out of over 20 formations, we select Utsira, Sandnes, and Stø to study. Real $CO_2$ storage projects are taking place in Stø and Utsira. Stø is also one of the (few) aquifers for which fault information is available. We use Sandnes to compare results against those from Utsira since their top-surfaces are quite different. We emphasize that we have not taken the geological history of these formations into consideration such as erosion and uplift, but simply use the datasets provided in the atlas, which in the simplest case consists only of top-surface and thickness maps and average rock properties. Given these simplifications, the numbers we produce should not be taken literally as true estimates for these specific formations.

Utsira and Sandnes are located in the Norwegian North Sea, and Stø is in the Barents Sea; see Figure 2. Utsira is from the uppermost middle Miocene to Quaternary age, and has an average top-surface depth of almost 800 meters (ranging from 300 to 1400 meters). Sandnes is from the lower Jurassic age, and has an average top-surface depth of approximately 2000 meters (ranging from 300 to 3400 meters). Stø is from the lower Jurassic age, has an average top-surface depth of approximately 2300 meters (ranging from 1400 to 3600 meters), and is part of the Hammerfest basin. Data quality for Utsira is considered good, Sandnes is considered limited, and parts of Stø are considered limited to good. ("Good" implies 3D seismic and well data are available from the actual formation, and "limited" implies 2D seismic is available, and well data comes from similar geological formations only (Halland et al., 2014)). The depth and thickness maps of Stø and Utsira come with a resolution of 500 by 500 $m^2$, while those for Sandnes come with a resolution of 1000 by 1000 $m^2$. Boundaries of the aquifers are considered open, unless information is given to indicate otherwise (e.g., a fault line exists along the southern and part of the northern boundaries of Stø, illustrated later in Figure 13). An open boundary means there is communication between the aquifer and whatever lies adjacent to it, be it another aquifer or the sea bottom.

For most of the aquifers, the atlas only reports average petrophysical properties; the average permeability and porosity of Utsira is reportedly 1000 mD and 0.2112, while that for Sandnes is 150 mD and 0.0875. However, we obtained heterogeneous rock data for the Stø aquifer of the Barents Sea via personal communication with the NPD. To formulate plausible heterogeneities for Utsira, we first derive a porosity-permeability relationship that fits the rock data for Stø; see Figure 3. As shown in the figure, porosity is approximately a linear function of depth, and permeability is a logarithmic function of porosity. Modifying Stø's porosity model to $\phi = \phi_0 - 5 \times 10^{-5}\,(z - \bar{z})$, where $\bar{z}$ is the average aquifer surface depth, yields a plausible porosity model for the Utsira aquifer with an average porosity close to $\phi_0 = 0.2$ (i.e., the average porosity given in the atlas). Then, using Stø's permeability model, the corresponding permeabilities in the Utsira geomodel range from 0.5 to 2.5 darcys, with an average of around 1 darcy (i.e., the average permeability given in the atlas). We note that a study on sand properties in Utsira has suggested that permeabilities could range from 1.1 to 5 darcys (Singh et al., 2010).

### *2.4. Storage capacity estimation*

A standard approach for estimating storage capacity in saline aquifers involves multiplying the aquifer's pore volume by a storage efficiency factor (U.S. Department of Energy, Office of Fossil Energy, 2015). This factor can be obtained by combining geological and laboratory measurements, past experience, and statistical techniques based on simplifying assumptions on the injection process. Another useful quantity to compute is the amount

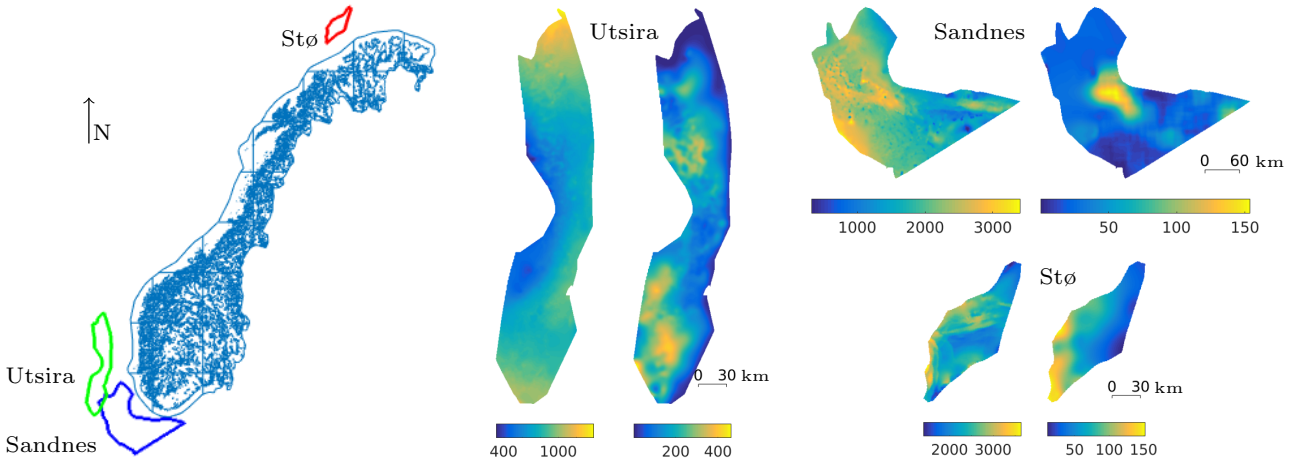


Figure 2: Formation geomodels considered in this work (Utsira, Sandnes, and Stø). *Left plot*: Approximate location along the Norwegian Continental Shelf. *Right plots*: Maps of geomodel depths (left) and thicknesses (right) in meters.

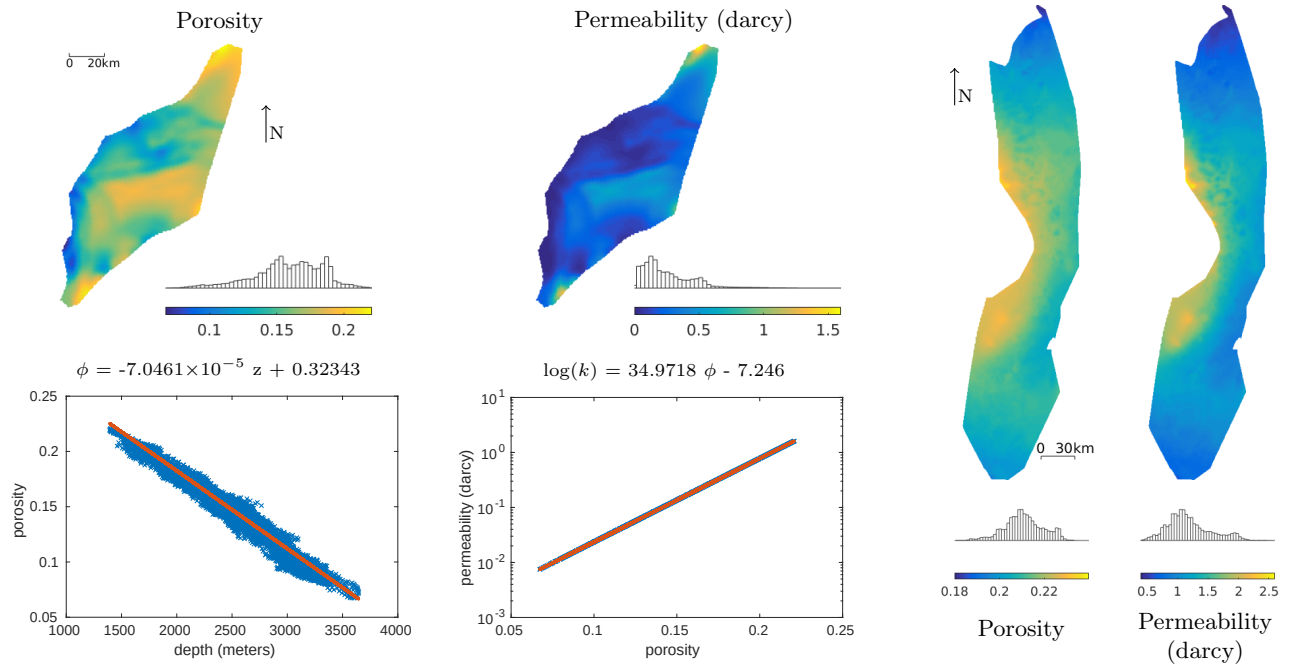


Figure 3: Heterogeneous rock properties. A porosity-permeability model is obtained from the Stø geomodel (left), and heterogeneous properties are created for the Utsira geomodel (right) using similar trends. Histogram of property values are included above each plot's colorbar, which helps illustrate the skewness and that the majority of permeability values are towards the lower end.

of $CO_2$ that may be stored in structural traps found within the aquifer's undulating caprock. For example, Zweigel et al. (2004) illustrates a structural trap and associated spill-point near the Sleipner injection site in the Utsira formation. Structural traps are analogous to inverted ponds or lakes found within a watershed: they each have their own catchment region that collects rainwater ($CO_2$) and channels it toward a body of water (local trap). As the pond or lake (trap) fills up to its spill-point, water ($CO_2$) will flow via rivers to an adjacent catchment region, until it becomes full and over-flows, and so on. These catchment regions, local traps, and connecting rivers can be identified by spill-point analysis; see Nilsen et al. (2015b) for algorithmic details. This concept is similar to secondary migration modelling of hydrocarbons presented in Sylta (2004), which has been applied to $CO_2$ storage modelling, e.g., Lothe et al. (2016). Once the geometric volume ($V_{\text{trap}}$) of each trap is found, the structural trapping capacity in terms of $CO_2$ mass is calculated by,

$$M = \int_{\Omega} \rho_{CO_2} V_{\text{trap}} \phi \left(1 - S_{\text{rw}}\right), \tag{5}$$

where $\rho_{CO_2}$ is $CO_2$ density at aquifer conditions, $\phi$ is porosity, and $S_{\text{rw}}$ is the residual water saturation; see e.g., Bachu et al. (2007). All terms in the integrand can be spatially varying fields. This is important since $CO_2$ found in a relatively shallow structural trap will have a much lower density than $CO_2$ found in a deep structural trap, and two traps with the same pore volume ($V_{\text{trap}}\phi$) can thus have vastly different mass storage capacities. While $CO_2$ is likely to also become trapped within the aquifer through residual, solubility, mineral trapping, using (5) to provide a static estimate for storage capacity is sufficient for the purposes of our work.

### *2.5. Forecasting $CO_2$ storage*

The trapping structure of an aquifer's top surface was briefly introduced above. Knowledge of this trapping structure can be used for more than just static capacity estimation. Consider, for example, the top-surface of a hypothetical, open aquifer shown in Figure 4 (top left plot). Imagine a plume of $CO_2$ located within the deeper elevations of this aquifer. If this plume were to be driven by buoyancy forces only, which is a reasonable assumption to make some time after injection has stopped and the induced pressure rise around the injection zone has dissipated, the trapping structure indicates that the plume will migrate up into trap X. Once trap X is filled, any more incoming $CO_2$ would spill over trap X and migrate into trap Y. By tracking this so-called *$CO_2$ spillage* along each spill-tree, we can predict how much $CO_2$ will remain stored within the aquifer and how much will eventually reach the boundary edge and then leak out of the open system. This forecasting method can also be used to estimate how $CO_2$ distributes in a closed system, but in this case, $CO_2$ will not leak across the boundary edges and global pressure buildup will impact the capacity within the traps (i.e., as pressure rises, $CO_2$ density increases, and thus traps can contain more $CO_2$ mass).

The rest of Figure 4 illustrates a migrating plume under a sloping and wavy top-surface. The $CO_2$ inventory reports how much is trapped, free, or leaked at any given time, as well as the amount of $CO_2$ predicted to remain trapped within the aquifer (blue dashed line). It takes some time before the forecast converges, for the following two reasons. First, aquifer pressure rises during the injection period, and takes some time to dissipate during the migration period. So, before migration is driven only by buoyancy forces, $CO_2$ can be driven by pressure gradients. This can cause additional spillage (or migration) from one spill-path to another and consequently structural trapping that cannot be predicted by a spill-point analysis from the injection point only; see bottom row in Figure 4. Second, as the plume migrates along a spill-path, it leaves behind an amount of residually trapped $CO_2$ within the pore space, which was unaccounted for by the forecast. The forecast does not account for solubility trapping either, so if we had included dissolution in our illustration, it is possible that we would need to simulate plume migration for a longer time before the forecast converges.

Once the forecast has converged, the simulation of plume migration can be exited. However, in this work, all model realizations are simply run for the same number of years which is sufficient for the pseudo-steady state to be reached. Further details of the trapping forecast can be found in Allen et al. (2017).

### *2.6. Fluid flow simulation*

As mentioned earlier, 3D flow simulation in large-scale aquifers is too time consuming when hundreds of simulations need to be performed for uncertainty or parameter sensitivity studies. To reduce computational time, we make a few simplifying assumptions. Because of large differences in fluid densities, strong buoyancy forces will cause the $CO_2$ and the formation fluid to segregate into two vertical layers almost instantly after $CO_2$ has been injected: lower density $CO_2$ is on the top and higher density brine is on the bottom. Secondly, because of the long time period and the large differences in horizontal and vertical extent of the aquifer, fluid flow in the vertical direction can be considered negligible compared with the horizontal flow. These two assumptions are the basis of *vertical-equilibrium* (VE) modeling, which is a method that dates back several decades, e.g., Martin (1958); Coats et al. (1971), and has more recently been re-introduced as a computationally efficient way

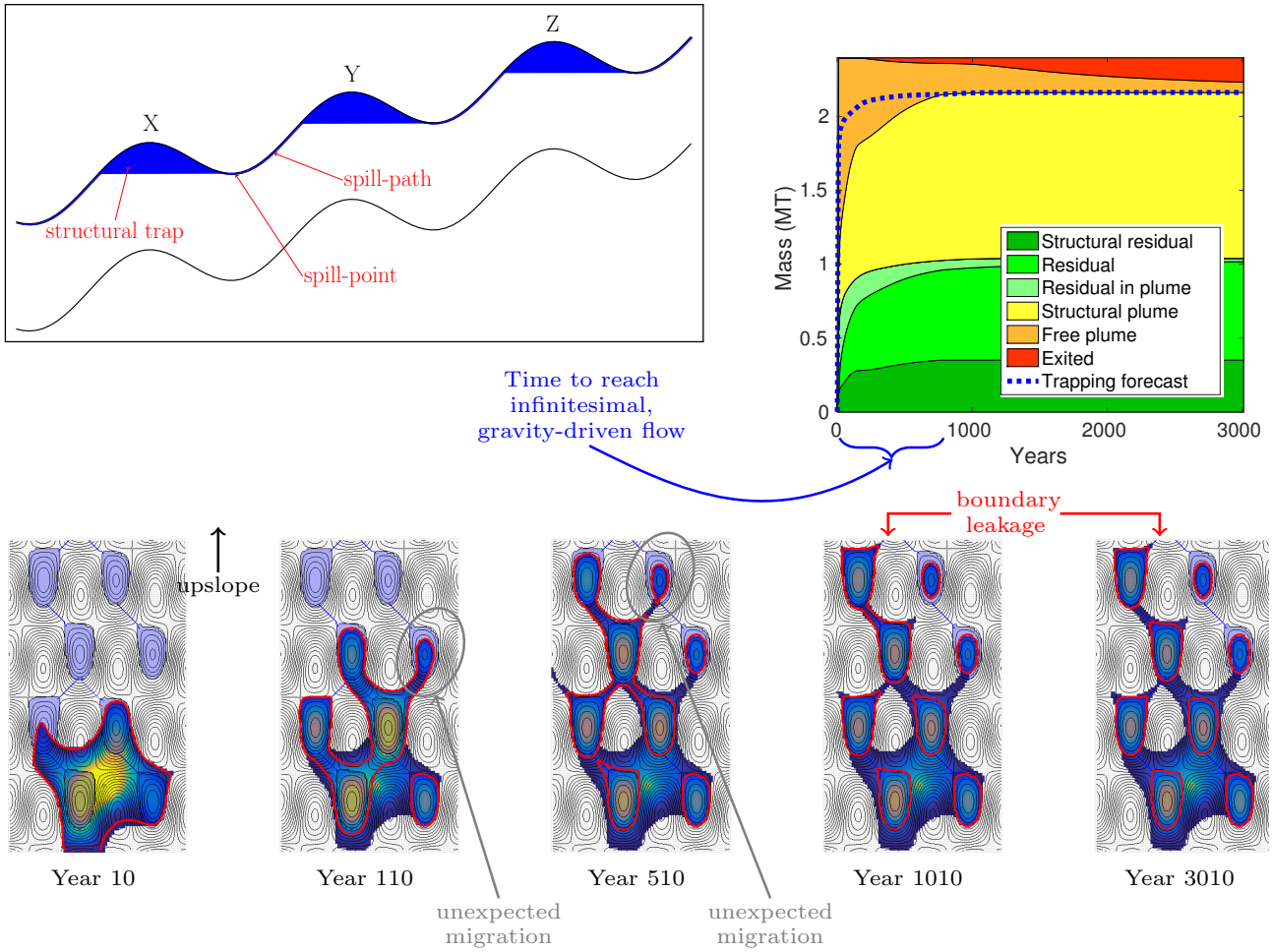


Figure 4: Convergence of the migration (or trapping) forecast. *Top left*: Structural traps and spill-path in a hypothetical aquifer's top-surface. An infinitesimal flow of $CO_2$ from a deeper elevation in the aquifer fills up trap X until $CO_2$ spills over the spill-point and migrates towards trap Y, etc. *Bottom row*: Migrating plume shown at select times under a sloping, wavy top-surface. Red outline indicates free (mobile) or structurally trapped $CO_2$, while any $CO_2$ outside of this red outline is residually trapped. Blue to yellow colours represent degree of $CO_2$ saturation (minimum of $s > 0.01$ to maximum of one minus residual water saturation of 0.11). *Top right*: Trapping inventory of $CO_2$ over the simulated time.

of studying long term migration in the context of $CO_2$ storage (e.g., Hesse et al. (2008); Gasda et al. (2009); Bandilla et al. (2012); Nordbotten and Celia (2012); Cihan et al. (2015); Nilsen et al. (2016a)). Herein, all simulations are performed using a VE model implemented in the open-source software MRST (MRST, 2017b), particularly the MRST-co2lab module (MRST-co2lab, 2017b). This VE model is formulated as a standard black-oil model, except that actual closure relationships like capillary pressure, etc., have a different interpretation. Details of the model formulation can found in Lie et al. (2016).

We now present the vertically-averaged flow equations to help explain the impact of a few parameters on the plume migration. We omit the full derivation here and refer readers to Nilsen et al. (2011); Bandilla et al. (2014); Nilsen et al. (2016b) for more details. Using $CO_2$ height (or plume thickness) $h$ under the caprock as a variable in the incompressible limit, the fractional-flow formulation of the mass conservation equation reads

$$\frac{\partial}{\partial t}(\phi h) + \nabla \cdot \left( f(h)\mathbf{u}_t + \frac{\lambda_g \lambda_w}{\lambda_t} k \Delta \rho g \nabla (z+h) \right) = q_t. \tag{6}$$

Here, $\phi$, $k$, and $z$ denote porosity, permeability, and top-surface elevation respectively, $\Delta\rho$ is the density difference between the fluids, and $g$ is gravitational acceleration. Individual and total fluid mobilities are given by $\lambda_g$, $\lambda_w$, and $\lambda_t = \lambda_g + \lambda_w$, respectively, $\mathbf{u}_t$ is the total flux, and $q_t$ are total sinks/sources. Assuming negligible fluid injection $q_t \approx 0$ and no background flow, and hence negligible total velocity $\mathbf{u}_t \approx 0$, setting $\lambda_g\lambda_w/\lambda_t = h/\mu_g$ and $\frac{\partial z}{\partial x} = \sin\theta$, where $\theta$ is the top-surface tilt, and assuming $\nabla^2 h << 0$, (6) is reduced from 3D to 1D in the direction $x$ of the main aquifer slope:

$$\frac{\partial h}{\partial t} + \frac{\partial}{\partial x}\left( \frac{k\Delta\rho g \sin\theta}{\mu_g \phi} h \right) = 0, \tag{7}$$

where $\phi$ was assumed to be constant. These approximations are valid for thin plumes moving upwards under a sloping top-surface and when gravity is the dominating driving force. Equation (7) is a prototype of a transport equation, where fluid velocity is given by

$$\mathbf{v} = \frac{k\Delta\rho g \sin\theta}{\mu_g \phi}. \tag{8}$$

The above relationship indicates how the ratio among certain parameters will affect the speed of the migrating $CO_2$ plume. This is also illustrated in Figure 5, which shows the impact that permeability, porosity, and caprock tilt have on plume migration in two different synthetic aquifers. After 10 years of injection followed by 100 years of migration in the smooth top-surface aquifer, the position of the plume front is farther upslope (from the injection point) when permeability or caprock tilt has been increased, and nearer to the injection point when porosity has been increased. The same observation can be made in the wavy top-surface aquifer, however geometric trapping retards plume migration and contains the $CO_2$ within the aquifer even after 300 years. On the other hand, the plume under the smooth top-surface has already left the (open) aquifer boundaries after 300 years because there is nothing to hinder its upslope migration.

The results illustrated in Figure 5 are consistent with previous findings from a number of studies on the topic. The impact of caprock tilt has been discussed in e.g., Gasda et al. (2006); Taku Ide et al. (2007); Espie and Woods (2014); Shariatipour et al. (2016). Also, the influence of caprock topography has been studied in e.g., Nilsen et al. (2012); Goater et al. (2013); Gasda et al. (2012, 2013), and a typical observation is that smooth top surface models underestimate capacity. In particular, Goater et al. (2013) demonstrated that in migration-limited storage cases, up to two times as much $CO_2$ could be stored when top-surface topography was introduced to an otherwise smooth caprock.

For the parameter uncertainty evaluations we perform in this work, (8) explains the main effects caused by changes in permeability and porosity. Perturbations in the top-surface topography of the type considered herein, will generally introduce additional small-scale traps. The effect of traps like this, appearing on a smaller scale than the $CO_2$ plume, are studied in detail in models in Gasda et al. (2012). Rugosity in the top surface will lead to local geometric trapping of $CO_2$, which is analogous to small-scale residual trapping; this local trapping retards the plume migration and eventually stabilizes the plume. The effect of this top-surface roughness is evident when plume heights are small.

## 3. Results and Discussion

In this section, we demonstrate the sensitivity of storage estimates to changes in porosity, permeability, caprock elevations, and aquifer conditions using a geomodel of the Utsira aquifer. The sensitivity of storage estimates to caprock elevations is also assessed using a geomodel of the Sandnes aquifer, and compared against

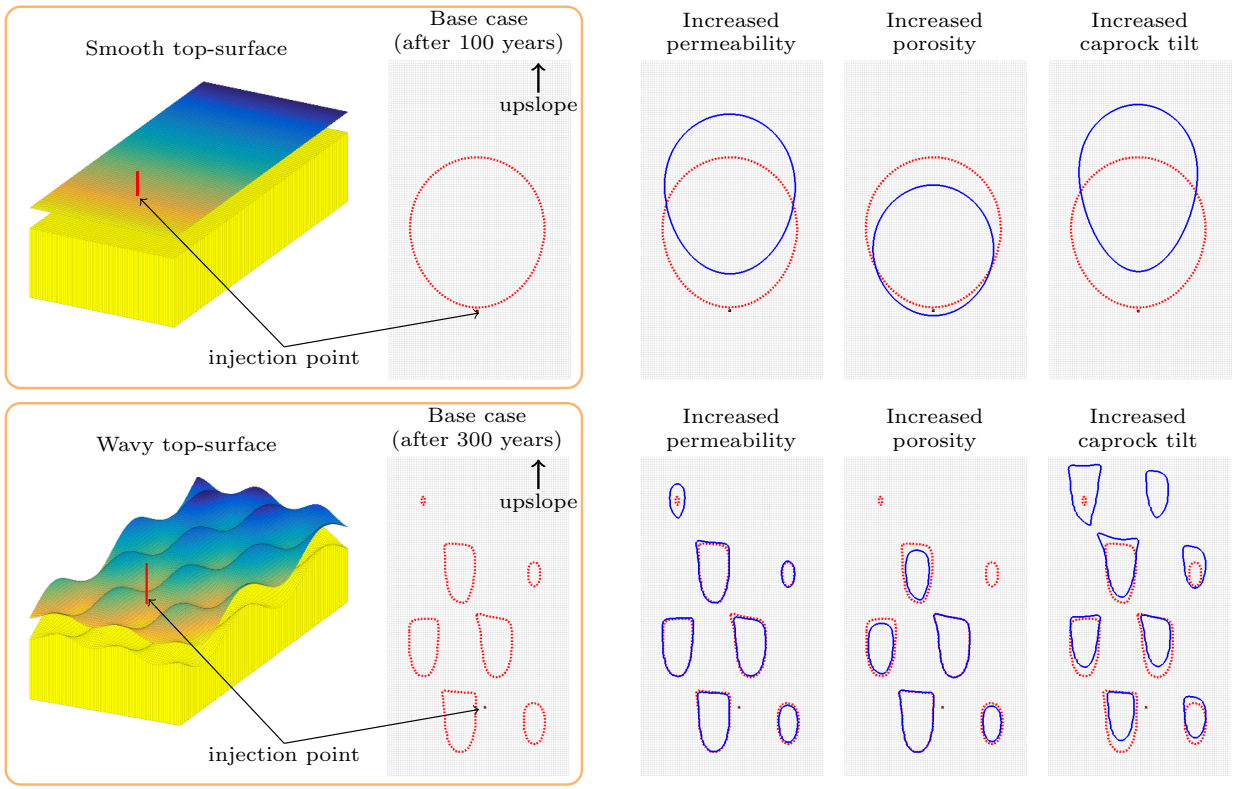


Figure 5: Impact of individual parameters on a migrating $CO_2$ plume in two different synthetic aquifer systems, one having a planar top surface and the other containing several structural traps. Plume position is shown after 300 years and 100 years of migration in the wavy and planar case, respectively. Red-dashed and blue lines depict simulated plume outlines given the base geomodel and modified geomodel, respectively.

Utsira. Likewise, we use a model of the Stø aquifer to demonstrate how plume migration and pressure buildup is sensitive to changes in fault transmissibilities. The discussion is subdivided into subsections that each focus on how the uncertainty of a particular parameter impacts either storage capacity estimation, plume dynamics, or the trapping forecast.

### *3.1. General setup*

Before discussing specific parameters, we explain the general set-up used to generate our results. Figure 6 shows how uncertainty in rock properties and caprock elevation impacts plume migration and trapping in the southern portion of the Utsira aquifer. The setup consists of a single injection point located in the south, from which 719 Mt are injected over a period of 30 years (i.e., $CO_2$ injection rate is 1 $m^3/s$ given a reference density of 760 $kg/m^3$). The left plot shows the trapping structure for the base model, with structural traps colored in light red, spill-paths shown as light red lines, and catchment regions associated with each trap colored in shades of gray. Heterogeneous porosity and permeability values were set using the method explained in Figure 3. The parameters were perturbed one at a time to investigate their individual impact on model responses. Porosity was first perturbed by a Gaussian field with values spanning the interval $\pm$ 0.05. The same perturbations were then applied to the permeability by using the logarithmic relationship between permeability and porosity, while porosity was reset to its original value. Caprock elevations were perturbed within an interval of $\pm$ 5 meters. For each perturbation, we performed a forward simulation for all hundred members of the ensemble to capture the final $CO_2$ plume after 3000 years of migration. (If the simulation period had been prolongated further, we would eventually notice more $CO_2$ exiting the domain's lateral boundaries.) The top row of Figure 6 shows the final plume outlines as blue lines for all perturbed realizations, with the plume outline predicted for the base case shown in red. The trapping inventory shows wedges for the base case, with error bars indicate the 10th and 90th percentile values of the ensemble. The forecast curve is shown by the blue dashed line, along with its error bars.

The magnitude of the perturbations will obviously impact the sensitivity of the plume dynamics to a particular parameter. Thus, we consider two additional perturbation *levels* for each parameter, which we refer to as low and high (the perturbation level just considered is referred to as medium). Results are presented in Table 1. Perturbation extremes (or corresponding range of permeability) are shown, along with the evolution

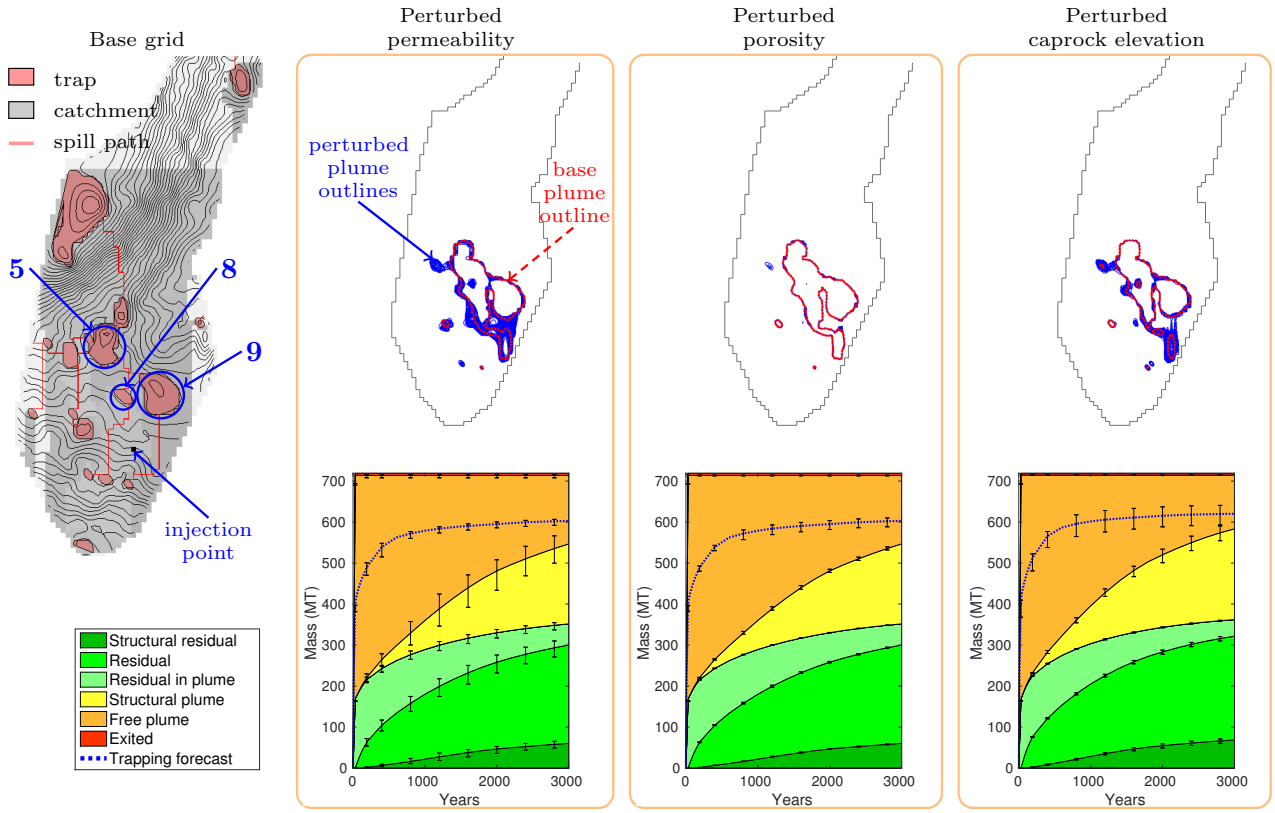


Figure 6: Impact of parameter uncertainty (permeability, porosity, and caprock elevations) on plume migration and trapping inventory. *Top row*: Ensembles of plume outlines after 3000 years of migration, compared to the base case (red dashed line). *Bottom row*: Trapping inventory with error bars along each trapping wedge, indicating 10th and 90th percentile wedge values of ensemble at a given point in time.

of the Sørensen–Dice coefficient computed using (4). More precisely, the curves illustrate the evolution of the ensembles' averaged values and standard deviation. The perturbation intervals are chosen somewhat arbitrarily, and are not meant to suggest the actual uncertainty ranges associated with this specific aquifer.

Static capacity estimates are also influenced by parameter uncertainty. In Table 2, we summarize the stochastic characteristics of the structural trapping capacity for Utsira-South in light of uncertain caprock elevations and porosity. Different perturbation levels were applied to these parameters. The resulting stochastic characteristics are reported in Figure 7 for a particular perturbation, which essentially shows a bell-shaped distribution in the ensemble space. Computing structural trapping capacity is not computationally intensive, thus a total of 1000 realizations were used for each ensemble space. Permeability is not included in this list because it only plays a role in plume migration and does not influence static capacity. Further discussion of these results is presented in the following subsections.

### *3.2. Porosity*

For a fixed volume of $CO_2$, variations in porosity will impact the total rock volume that the plume comes in contact with. Increasing the pore volume reduces the total rock volume the plume occupies, which slows down the migration so that the plume does not travel as far upslope. We illustrate this in Figure 5. Increasing porosity also impacts the amount of $CO_2$ that will become residually trapped within the pore grains as the plume moves through the pore space.

The situation is a little different when the porosity is perturbed by a random Gaussian field. In some regions, the plume migration will slow down because of increased porosity, whereas the plume will migrate faster in other regions where the porosity is decreased. In general, the combined effect may lead to significant changes in migration. In our particular case, however, a porosity perturbation of $\pm$ 0.05 barely changes the plume outline as shown in Figure 6. Regardless of the realization, the plume outline consists of a region that has been swept on its way to fill traps, as well as a few filled or semi-filled traps (traps number 5, 8, and 9 in the plot). Whereas Traps 8 and 9 are fully filled in every realization, Trap 5 varies from being 60% to almost 90% filled. This implies that the injected plume does not have a sufficient amount of $CO_2$ to completely fill the upslope traps, and hence the footprint of the plume remains almost identical irrespective of Trap 5's degree of

Table 1: Perturbation level versus impact on flow and migration in Utsira South. Inset figures show the evolution of the mean ($\mu$) and one standard deviation ($\sigma$) of the Sørensen–Dice coefficient (y-axis) from 30 to 2800 years (x-axis) for 100 realizations for the geomodel.

| | Perturbation level (or parameter range) and results | | | | | |
|---|---|---|---|---|---|---|
| Parameter | Low | | Medium | | High | |
| caprock depth (meters) | ± 1 | 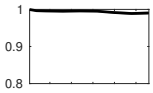 | ± 5 | 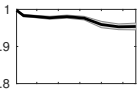 | ± 15 | 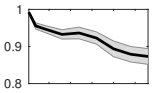 |
| porosity (unitless) | ± 0.02 | 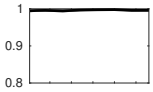 | ± 0.05 | 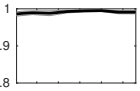 | ± 0.10 | 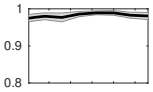 |
| permeability (darcy) | [0.32, 2.18] | 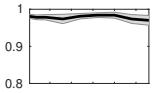 | [0.15, 4.96] | 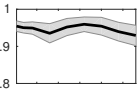 | [0.03, 25.67] | 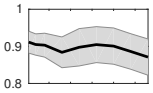 |

Table 2: Impact of parameter uncertainty on structural trapping capacity estimate. Symbols: mean ($\mu$), one standard deviation ($\sigma$), coefficient of variation (cov=$\sigma/\mu$), 10th percentile (P10), 90th percentile (P90). Each ensemble space consists of 1000 realizations.

| | Structural trapping capacity (Mt) | | | | | | | | |
|---|---|---|---|---|---|---|---|---|---|
| Parameter | $\mu$ | median | $\sigma$ | cov | P10 | P90 | max | min | spread |
| caprock depth | | | | | | | | | |
| ± 1 meter | 608 | 607 | 5.4 | 0.9% | 601 | 615 | 624 | 591 | 34 |
| ± 5 meters | 607 | 607 | 25.5 | 4.2% | 576 | 639 | 691 | 526 | 165 |
| ± 15 meters | 614 | 612 | 68.2 | 11.1% | 529 | 702 | 831 | 402 | 429 |
| porosity | | | | | | | | | |
| ± 0.02 | 592 | 592 | 6.1 | 1.0% | 584 | 600 | 612 | 571 | 41 |
| ± 0.05 | 592 | 593 | 15.2 | 2.6% | 573 | 612 | 643 | 540 | 103 |
| ± 0.10 | 592 | 592 | 30.1 | 5.1% | 554 | 632 | 694 | 488 | 206 |

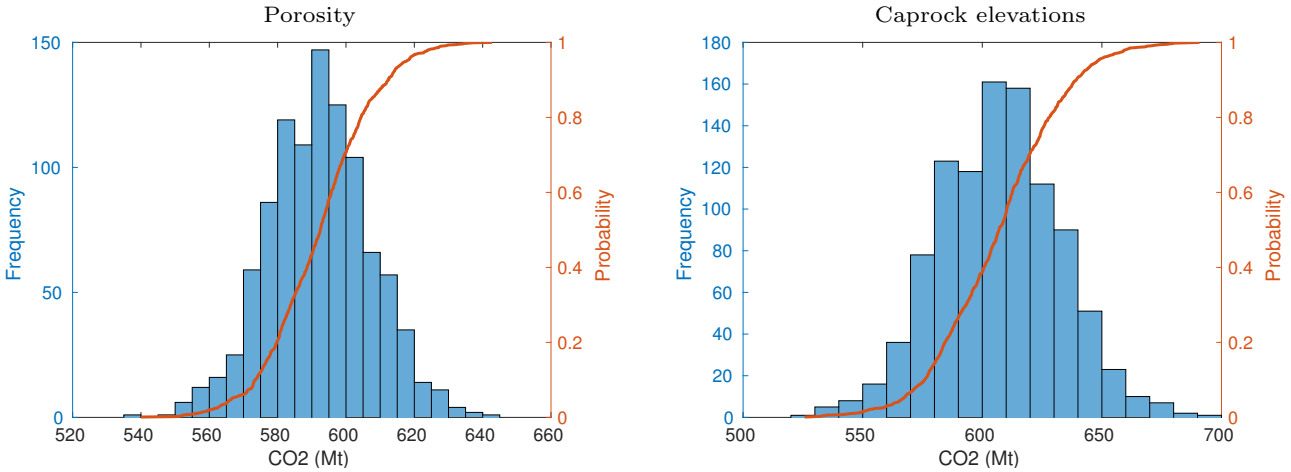


Figure 7: Histogram and cumulative distribution function of an ensemble of structural trapping capacities, corresponding to a porosity and caprock elevation perturbation of ± 0.05 and ± 5 meters, respectively.

filling. Table 1 shows that increasing the perturbation level to ± 0.10 results in a slightly worse similarity index (Sørensen–Dice coefficient) during the migration years; this implies that perturbing the porosity does indeed influence the migrating plume, even if only to a very small degree.

Regarding static capacity estimates, we notice from Table 2 that uncertainties in porosity has a slight effect. Since the average porosity in the base geomodel was around 0.2, a perturbation level of ± 0.10 implies an uncertainty of up to ≈ 50% of the base case. Despite such a high uncertainty, the ensemble's coefficient of variation is only 5%.

### *3.3. Permeability*

Permeability affects the dynamics of the system by changing the speed of a migrating plume, resulting in a thinner plume that reaches farther upslope; see Figure 5. Its influence on the direction of a migrating plume is expected to be less significant compared to caprock topography, which influences traps and the direction of the spill paths.

Manceau and Rohmer (2016) assessed the sensitivity of $CO_2$ migration to several input parameters including porosity and (absolute) permeability. For the case they studied, permeability was found to be more impactful than porosity on the total mass of mobile $CO_2$ (i.e., the free plume) and on how far this free plume migrates away from the injection point. While their approach accounted for interaction effects and here we perturb one parameter at a time, Figure 6 illustrates how, when using the logarithmic relationship between porosity and permeability observed in Figure 3, variations in permeability impact plume migration much more than the variations in porosity. Not only are the perturbed plumes visually different from the base case, but the trapping inventory also shows a larger spread in wedge values, such as the amount of $CO_2$ in the free plume. These wide error bars do not necessarily indicate that the final storage amount will differ as much from the base case, rather it simply means different amounts of trapping are occurring at different points in time. Indeed, the forecast curve exhibits a very small spread (between the 10th and 90th percentile values), and the majority of the forecasts in the ensemble suggest that approximately 600 Mt of $CO_2$ will remain in the aquifer (or 119 Mt will eventually leak), similar to the base case forecast.

In Table 1, a parameter range is given for permeability. Recall that we perturbed permeability by first perturbing porosity and then using a logarithmic relationship between these two rock properties, before setting porosity back to its original value. As such, we state the minimum and maximum value of the perturbed permeabilities since the maximum changes are not centered around an average value. Note that the use of a logarithmic relationship to compute the permeability field leads to some unrealistically high values (25 darcys), but these are limited to a few isolated grid cells. Perturbing permeability results in a wider spread in the Sørensen–Dice coefficient (SDC) curves for all three perturbation levels, compared to perturbing porosity or caprock elevations. Also, the mean SDC value of the ensemble at 30 years is below 1, indicating that plumes are already dissimilar from the base plume by the end of the injection period.

### *3.4. Caprock elevations*

Because of the large density difference between $CO_2$ and brine, $CO_2$ behaves like a thin plume traveling underneath the aquifer's undulating caprock. As such, the topography of the aquifer's top surface is the main parameter dictating the migration direction and the overall plume shape. For example, Figure 6 illustrates that caprock perturbations in the Utsira geomodel can have a significant impact on plume migration. Also, the error bars on the trapping inventory wedges suggest that plume migration becomes more dissimilar as time goes on.

Table 1 shows that by approximately 3000 years, the mean values of the caprock and permeability SDC curves are quite similar. Since the slope of the SDC curves for caprock and permeability are different, it is possible that we would eventually notice larger dissimilarity due to caprock perturbations than due to permeability if we studied a longer migration period. This observation agrees with a finding made in Manceau and Rohmer (2016) regarding how the impact of an individual parameter (especially absolute permeability) on plume migration can evolve over time, becoming either more or less important than other parameters.

Caprock topography is determined using seismic surveys, and thus the real uncertainty in top-surface elevations is likely related to aquifer depth. Without knowledge of the uncertainty associated with a particular geomodel, we have chosen to apply an arbitrary degree of perturbation to a given surface model. (This perturbation is applied to the entire top-surface, although we recognize that there is likely more uncertainty in one part of the study area than in other areas.) Obviously, the same level of perturbations can have largely different effects on migration, depending upon the topography of the top surface. To illustrate this point, we compare the static trapping capacity of two aquifers that have very different caprock topographies: the full Utsira geomodel and the Sandnes geomodel. For computational efficiency, we used coarsened versions of these geomodel grids, at a resolution of $2 \times 2$ km$^2$ for both grids. A range of perturbation levels from ±1 meter to ±30 meters were applied to the respective top surfaces. The mean trapping capacity and standard deviation

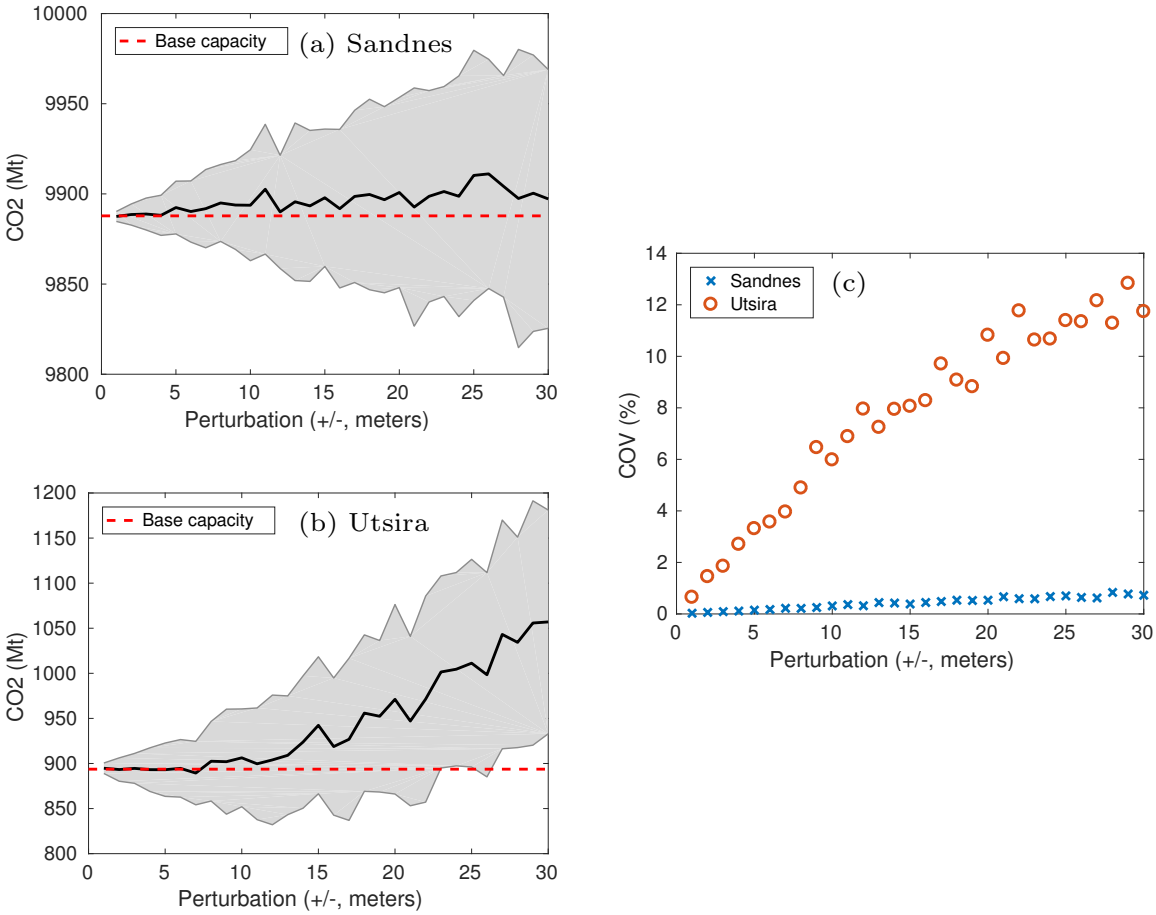


Figure 8: Impact of perturbation level on $CO_2$ trapping capacity. *Plots (a) and (b)*: Solid black line denote mean trapping capacity ($\mu$) and width of gray shaded area is one standard deviation ($\sigma$) of the ensemble at each perturbation level. Red dashed line is trapping capacity of base grid (no perturbation applied). *Plot (c)*: Coefficient of variation (COV=$\mu/\sigma$) versus perturbation level.

of each ensemble are plotted in Figure 8. The Sandnes aquifer contains dramatic slopes and a high degree of variation in the top surface. Increasing the perturbation level therefore only resulted in a very slight divergence between the base capacity and the mean trapping capacity of each ensemble. The Utsira surface model is relatively smooth compared to Sandnes, and its structural traps are sparsely distributed throughout the aquifer. Once perturbations reach approximately ±8 meters, the mean trapping capacity in the Utsira grid therefore diverges significantly from the base. Whereas a perturbation level of ±30 meters is not enough to produce a noticeably different trapping structure in the Sandnes geomodel (see Figure 9), it is easy to notice new traps in the Utsira geomodel, especially in areas where the elevation gradient is relatively smooth.

As mentioned, the grids used in the example discussed above were coarsened. Coarsening the grid affects the number of structural traps found in the top surface model and the storage capacity estimate. More specifically, small traps will disappear from the top surface when the grid is coarsened, as demonstrated in Nilsen et al. (2015a) for another North Sea geomodel. As such, we recognize that the storage estimates we presented in Figure 8 and 9 are specific to our grid resolutions, and we can expect higher storage estimates if finer grids were used.

We now look more closely at how uncertainty in caprock elevation affects long-term plume migration; see Figure 10. Here, we used a perturbation level of ± 15 meters, but instead of heterogeneous rock properties, a homogeneous porosity and permeability of 0.21 and 1 darcy, respectively, were used to emphasize the impact of topography. Also, instead of simulating an injection period (to reduce CPU time), the aquifer is initialized with hydrostatic pressure and a circular plume of 18 km in diameter containing 680 Mt $CO_2$. The migrating plume in the base geomodel is shown as red dashed lines, and the perturbed cases as solid blue lines. The discrepancy between the base results and the perturbed realizations increases as the plumes evolve. As shown in the figure, the Sørensen–Dice coefficient equals unity at $t = 0$, which indicates a perfect match, and becomes smaller than unity as the plumes evolve. Histograms taken at selected times (100, 1000, 5000, and 15 000 years) show a decreasing mean value as well as a larger standard deviation (and larger spread in values). It is interesting to note that the Sørensen–Dice coefficients for all realizations *generally* decrease in value. However, in some

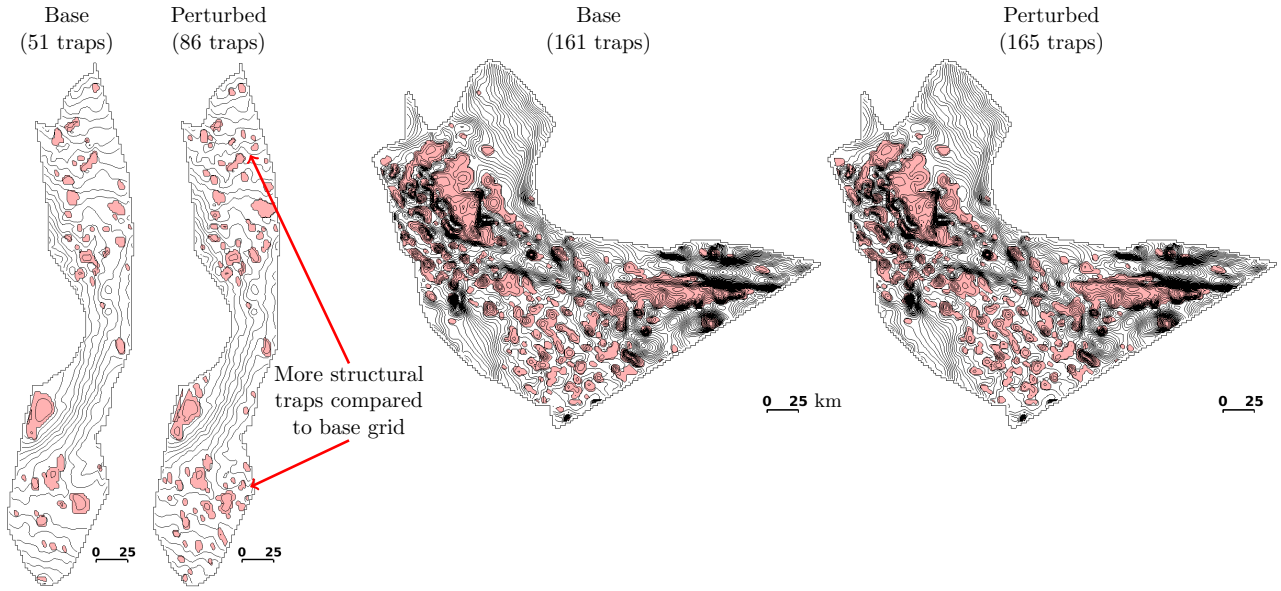


Figure 9: Impact of ± 30 meter perturbation on the trapping structure. *Left*: Trapping structure in Utsira's base grid and in the grid that gives a trapping capacity equal to the ensemble's mean trap capacity. *Right*: Sandnes base grid and the mean trap capacity grid. All contour lines are drawn at 50 meter intervals, and all grids are drawn using the same scale (scale bar indicates 25 km).

realizations the coefficient decreases and then increases over time. This implies that the plume migration may be very different from the base case at a given point in time, but then the discrepancy decreases as the migrating plume converges towards that of the base case. The Sørensen–Dice curve for two different realizations can cross over each other, which again indicates nonlinear and dynamic plume behavior.

The trapping inventory in Figure 10 shows that there still exist free (mobile) plumes in the base geomodel after 15 000 years (orange wedge in inventory). However, the total amount trapped shown as green residual and yellow structural wedges is hardly increasing at this point in time. Thus, it is safe to assume that the remaining free plume will simply migrate towards the open boundary and leak from the aquifer, i.e., the free plume (orange wedge) will be depleted as the amount leaked (red wedge) increases. In fact, after about 3000 years, the trapping forecast could adequately predict that approximately 615 Mt of $CO_2$ would ultimately remain trapped within the aquifer, and the remaining 100 Mt would leak. (Note that this study neglects both solubility and mineral trapping, but if they had been included in our example, it is likely that the amount that could eventually leak would be significantly reduced, potentially to zero.) We thus continue our investigation of how caprock uncertainty effects the model response by simulating only 3000 years of migration to capture long-term trapping/boundary leakage. Forecast results are shown in Figure 11 for four different perturbation levels: ± 1, 5, 15, and 30 meters. These forecasts correspond to the injection of 719 Mt of $CO_2$ through one fixed injector, over a period of 30 years. From the results, we first notice that a perturbation of ±1 meter does not produce noticeably different plume outlines in comparison to a perturbation of 15 or 30 meters. The forecasts for the ±1 meter predict that between 608 to 627 Mt of the injected $CO_2$ will remain in the aquifer. A perturbation level of 30 meters, on the other hand, suggests that between 518 to 715 Mt will remain trapped. Despite this wider variation, we notice from the histogram of final forecast values in the bottom right corner that the values do not take on a bell-shaped distribution, rather a larger percentage of the forecast values are towards the upper limit of 719 Mt (i.e., no $CO_2$ will leak). This skewed distribution indicates that a perturbation level of ±30 meters has created new traps and thus enhanced the storage capacity in most of the realizations. In other words, a higher degree of top surface rugosity leads to more structural trapping, which has been demonstrated in previous work, e.g., Nilsen et al. (2012); Gasda et al. (2013), and which we alluded to in Section 2.6.

Once again, grid resolution plays a role in our long-term migration results. For computational efficiency, the simulations discussed above were performed using a coarsened version of the geomodel (i.e., 2000 × 2000 $m^2$). With the full resolution (500 × 500 $m^2$), more small-scale traps are resolved and somewhat higher structural trapping will be observed. Likewise, the increased rugosity of the top surface will retard plume migration and potentially increase residual trapping. As noted in Nilsen et al. (2012), coarsening produces a smoother top surface that overestimates plume migration.

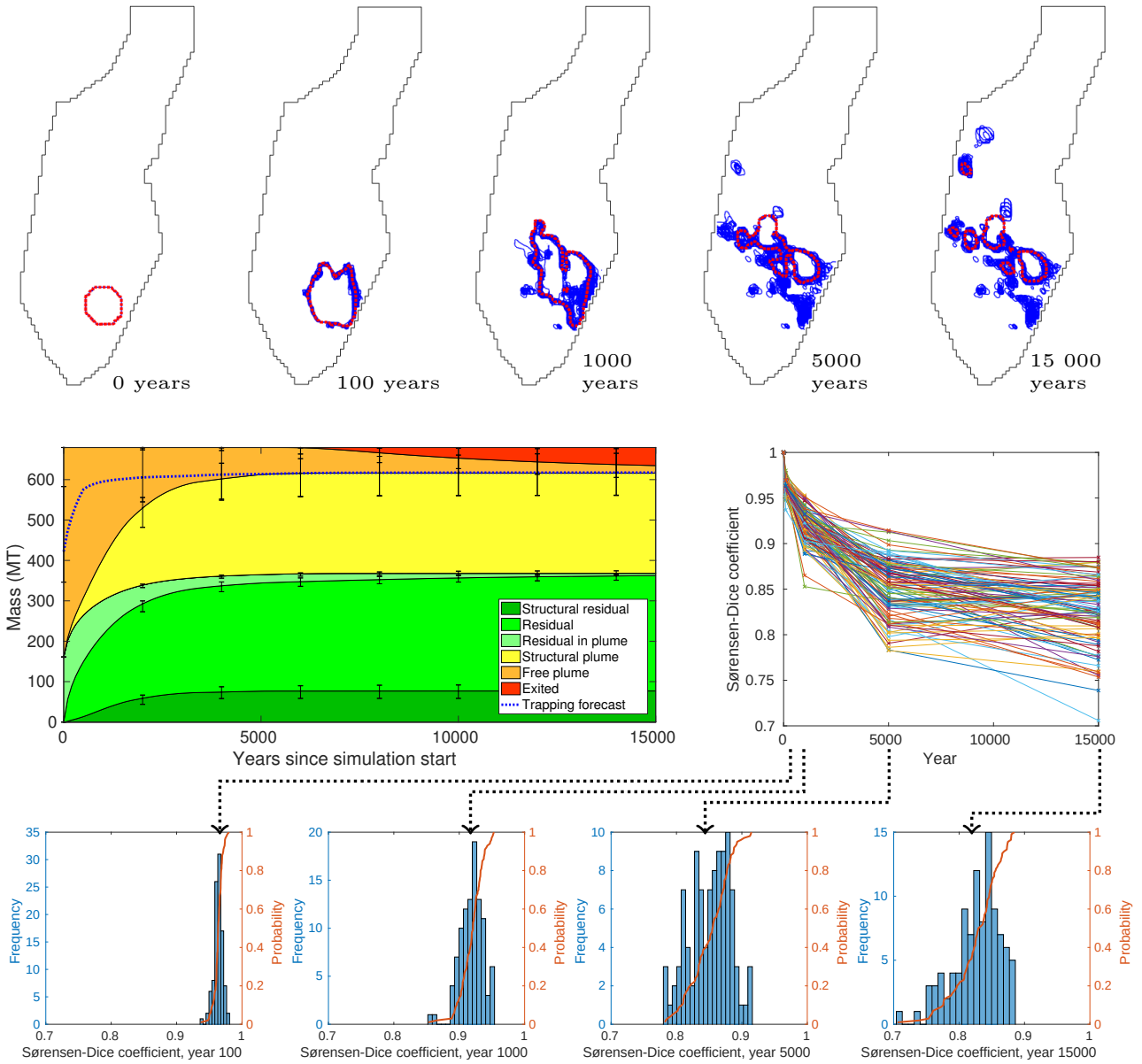


Figure 10: Impact of uncertainty in caprock elevations on plume migration and trapping inventory. *Top row*: snapshots of plume outlines simulated using perturbed geomodels (blue lines) and original geomodel (red dashed line). *Middle row*: wedges of trapping inventory with error bars showing 10th and 90th percentile values from all realizations, and evolution of the Sørensen–Dice coefficient from all realizations. *Bottom row*: histograms of Sørensen–Dice coefficients for all realizations taken at selected times.

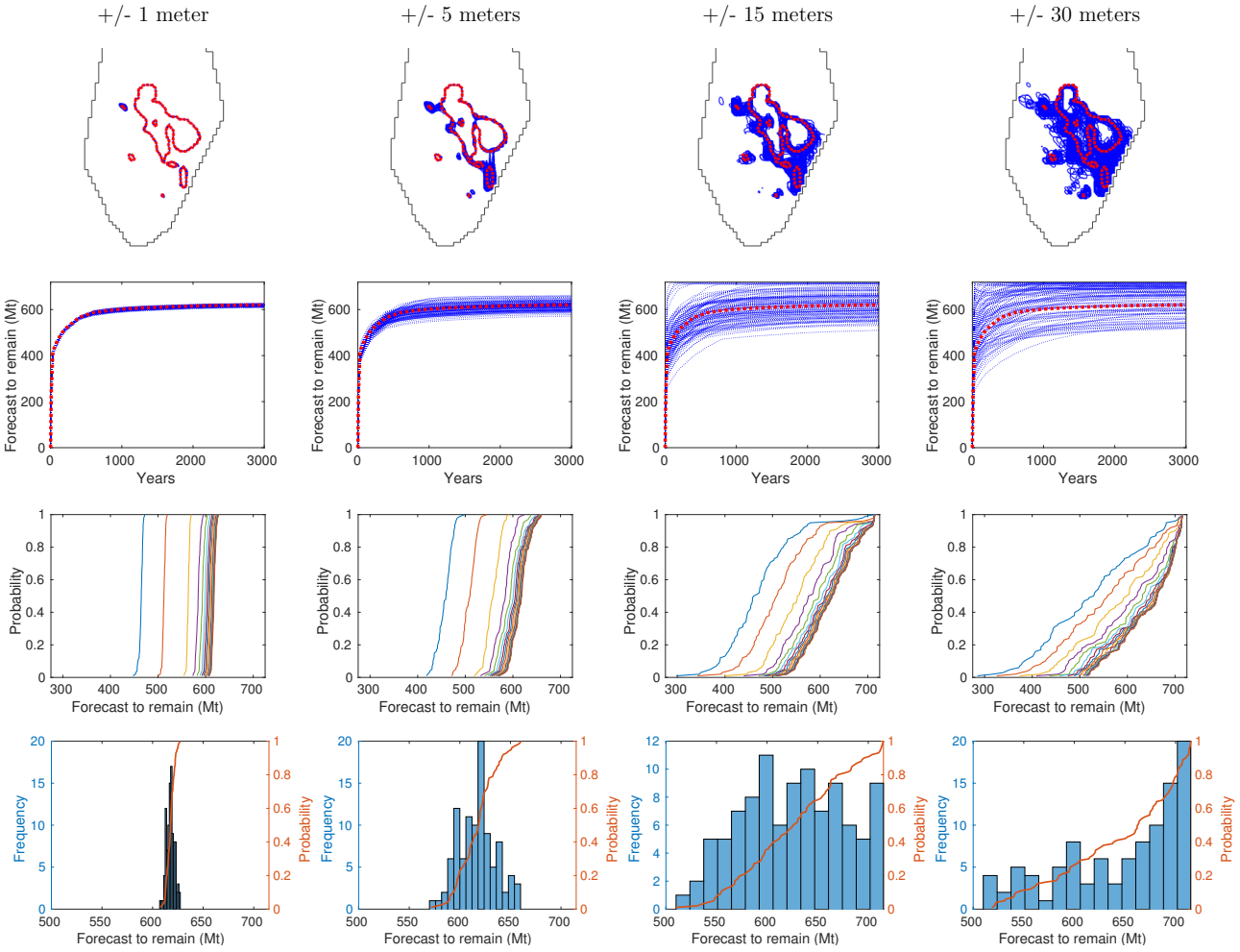


Figure 11: Impact of caprock elevation perturbations on trapping forecast. *Left to right columns*: results given perturbations of 1, 5, 15, and ± 30 meters. *Top row*: $CO_2$ plume outlines after 3000 years for base case (red) and perturbed cases (blue). *Second row*: Forecast curves of perturbed cases (blue) and base case (red). *Third row*: Cumulative distribution function of forecasts taken 100, 200, 400, 600, ..., 3000 years after the start of simulation. *Fourth row*: Histogram of forecasts taken at 3000 years.

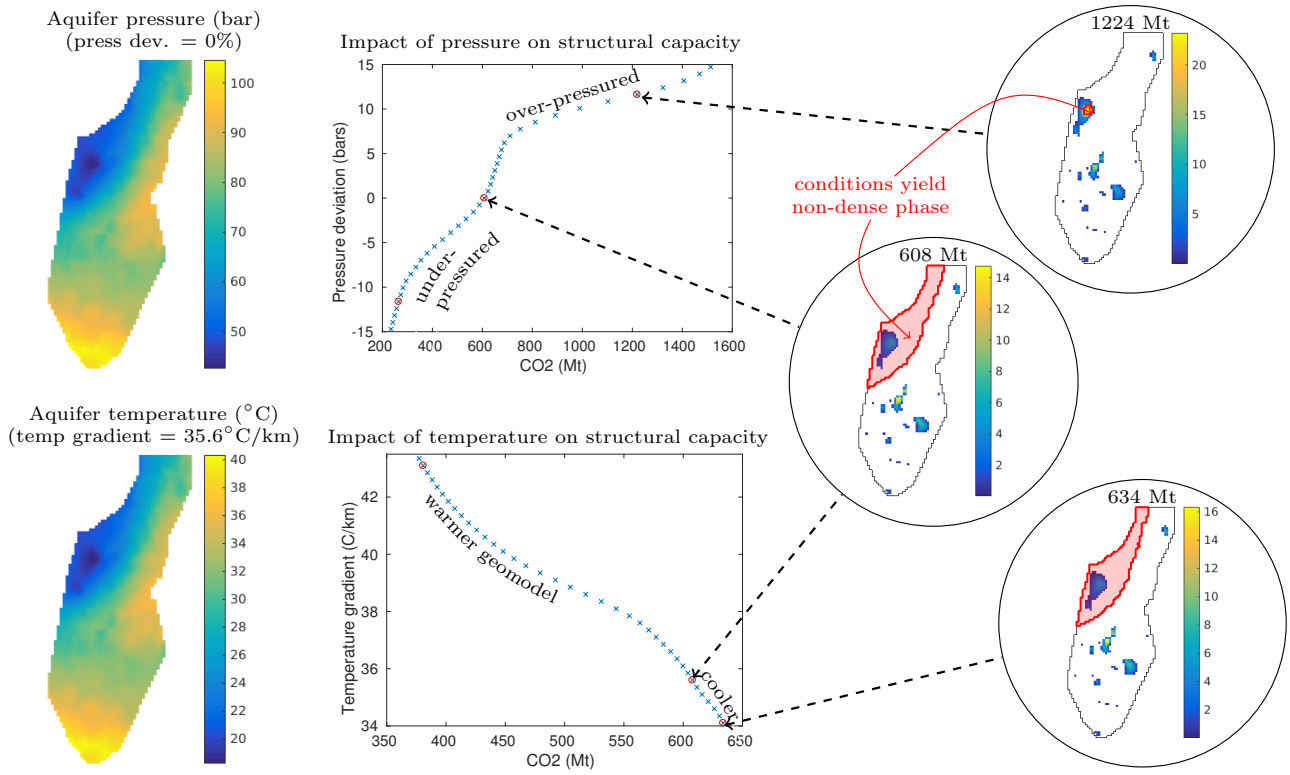


Figure 12: Representations of pressure and temperature uncertainty. The reference pressure (hydrostatic) is uniformly deviated by a percentage of its pore-volume weighted average, and the temperature gradient used to compute caprock temperature is varied. *Left*: Pressure and temperature conditions in the base model. *Middle*: Impact of pressure or temperature on structural trapping capacity. When pressure is varied, thermal gradient is fixed at 35.6°C/km, and when thermal gradient is varied, pressure is fixed as hydrostatic (i.e., no pressure deviation). *Right*: Trapping capacity of formation for select aquifer conditions. Colorbars are in units of megatonnes of $CO_2$. Red shading indicates conditions where $CO_2$ is *not* in its "dense" phase.

### *3.5. Initial aquifer conditions*

The influence of aquifer conditions (pressure and temperature) on $CO_2$ density and storage suitability has been discussed previously, e.g., Bachu (2003); Metz et al. (2005). Here, we investigate the impact uncertainty in aquifer conditions has on static capacity estimates for the Utsira aquifer. While we do not know the exact level of uncertainty associated with the initial conditions, we note that Gasda et al. (2017) calculates a maximum sustainable over-pressure of 15 bars for Utsira based on horizontal stress, and that Cavanagh and Haszeldine (2014) consider a temperature of 31 and 37°C for an Utsira layer (i.e, Sleipner layer 9) at 800 meters deep. This temperature range equates to a temperature gradient of 34 and 43°C/km, respectively, based on our assumed values for seafloor depth and temperature. In light of these pressure and temperature values reported by others, we first deviate hydrostatic pressure uniformly from -20% to 20% of its pore-volume weighted average, which corresponds to a deviation of roughly -15 to 15 bars since the average pressure for this geomodel is approximately 80 bars (recall (2)). Then, we deviate the caprock temperature by considering thermal gradients ranging from 34 to 43 C/km (recall (3)). Such a temperature deviation could be a result of variations in seafloor depth (which is assumed to be constant) and uncertainty in seafloor temperature and subsea thermal gradient. Deviating the pressure implies the aquifer is either under or over-pressured relative to the hydrostatic condition. An under-pressured or over-pressured aquifer could be a result of geological events such as burial or uplift, respectively. Also, production of fluids from the formation can cause under-pressure. The pressure and temperature deviation range we introduce here are intended as examples, and should not be understood as an in-depth assessment of actual geological conditions at Utsira. For some perspective, Alnes et al. (2011) presents formulas for Utsira's pressure and temperature profiles with an error range of ±0.2 bars and ±0.5°C, which is a much smaller window of variability than we are investigating here. Results are shown in Figure 12.

A few things can be said based on the results shown in Figure 12. Firstly, the base model suggests that approximately 608 Mt of $CO_2$ could be contained within the structural traps when pressure is purely hydrostatic and when aquifer temperature is based on a temperature gradient of 35.6°C/km. As pressure increases from a hydrostatic condition, $CO_2$ density increases and thus the structural traps can contain more $CO_2$. For example, when pressure deviates from hydrostatic conditions by approximately +11.5 bars, (or +15% of its pore-volume weighted average), the structural capacity of the geomodel increases to 1224 Mt. The opposite is true when

pressure drops lower than its hydrostatic state. Likewise, the structural storage capacity increases when a cooler geomodel is assumed (e.g., a temperature gradient of 34°C/km and hydrostatic pressure yields a structural storage capacity of 634 Mt), and decreases when a warmer geomodel is assumed, a finding that agrees with previous work, e.g., Bachu (2003). Secondly, we notice that structural storage capacity is nonlinearly related to either a change in pressure or a change in temperature. The reason for this is attributed to the fact that $CO_2$'s phase diagram shows a nonlinear relationship between $CO_2$ density and Utsira-South's aquifer conditions that range from 15 to 50°C and 20 to 160 bars. Within these intervals, the $CO_2$ density *increases* with increasing pressure and a fixed temperature, whereas the $CO_2$ density *decreases* with increasing temperature and a fixed pressure; see variation of $CO_2$ density with pressure and temperature given in Bachu (2003). Close to the critical point (31°C and 73.8 bars), slight changes in either pressure or temperature lead to significant changes in density. Thirdly, Utsira-South's aquifer conditions do not always cause $CO_2$ to be found in its "dense" phase (notice areas shaded in red in Figure 12), which we define as the combined liquid and supercritical regions in the phase diagram. Aquifer conditions have essentially been computed as a function of depth. The southern portion of the Utsira geomodel is located between depths of approximately 395 to 1040 meters. Within this range of depths, there is a point at which $CO_2$ changes from non-dense (i.e., gaseous phase) to its dense state. At any elevation deeper than this point, $CO_2$ will exist in its dense form.

### *3.6. Faults*

We use fault information that is available for the Hammerfest Aquifer Basin (provided to us by the Norwegian Petroleum Directorate) to investigate the impact that fault uncertainty has on plume migration. Figure 13 shows the faults present in this aquifer, which contains the Stø formation. A close-up view of the Stø geomodel, which was constructed based on top surface elevations and formation thickness, is shown on the right. The fault data are given as line coordinates, and had to be projected onto the Cartesian grid representing the geomodel. Thus, the line coordinates of the faults are represented discretely in the geomodel, and appear as stair-step fault lines corresponding to a continuous segment of cell faces in the right plot. While this is admittedly a simplistic representation of faults, we consider it adequate for illustrating our methodology here.

For this example, we treat the faults in Stø as either sealing, semi-sealing, or fully conducting. This treatment is achieved by multiplying the transmissibilities of the fault faces by a factor $\alpha = 0$ for sealing faults, $\alpha = 0.01$ for semi-sealing faults, and $\alpha = 1$ for conducting faults (i.e., leaving the transmissibilities unchanged). To emphasize the role of the faults, an array of injection wells are placed on the deeper side of two specific faults. We assume the aquifer has open boundaries, however the southern boundary and a portion of the northern boundary are fault lines. We simulate an injection period of 50 years with various injection rates followed by a post-injection period of 3000 years.

Figure 14 illustrates over-pressure and $CO_2$ saturations for the three fault cases, given an injection rate of approximately 0.25 Mt/year per well. The top row plots show over-pressure at a particular year during the injection period when the maximum over-pressure was reached. As expected, faults that limit the transmission of fluid cause pressure to buildup much more than in the case when faults are neglected, and the pressure becomes compartmentalized in parts of the aquifer. Approximately 3000 years after the end of injection, the pressure in all three cases has dissipated enough that it almost resembles the initial hydrostatic condition (not shown for brevity). This is not surprising, given our assumption that the aquifer has open boundaries along most of its perimeter. The bottom row plots show $CO_2$ saturations after 3000 years. There is only a slight difference between the $CO_2$ plumes in these fault cases. In the conducting fault case, $CO_2$ is not hindered and thus migrates upward and southward from Wells 1 to 5 where it collects in the shallow traps. In the sealing fault case, $CO_2$ migration is more hindered and thus does not reach these higher elevations. $CO_2$ migration in the semi-sealing fault case is somewhere in between.

Figure 15 shows the effect of injection rate on the maximum over-pressure simulated in the aquifer during the simulated period. Injection rates were varied from approximately 0.25 to 2.5 megatonnes per year. We note that some of these injection rates lead to an over-pressure that is likely not sustainable in the aquifer since they would cause stress induced rock failure. The minimum overburden pressure of this aquifer is calculated to be roughly 220 bars (using a formula presented in Nordbotten and Celia (2012) and assuming a sea-depth of 330 m, sea and formation water density of 1000 kg/m$^3$, and that the media lying above the aquifer is comprised of sandstone with a dry bulk density of 2000 kg/m$^3$ with a porosity equal to that of the aquifer's). The minimum initial (hydrostatic) pressure of the aquifer is 150 bars. As such, a conservative limit for the over-pressure should be less than 70 bars, otherwise the overburden pressure would be reached. This limit means the injection rates should be less than 0.4, 0.7, or 1.1 Mt/yr for a sealing, semi-sealing, or conducting fault assumption, respectively, which corresponds to a storage capacity of no more than 20, 35, or 55 Mt for this hypothetical 50 year injection scenario. These numbers should not be taken literally as true capacity estimates, but rather this example demonstrates how much estimates can vary given the uncertainty of faults.

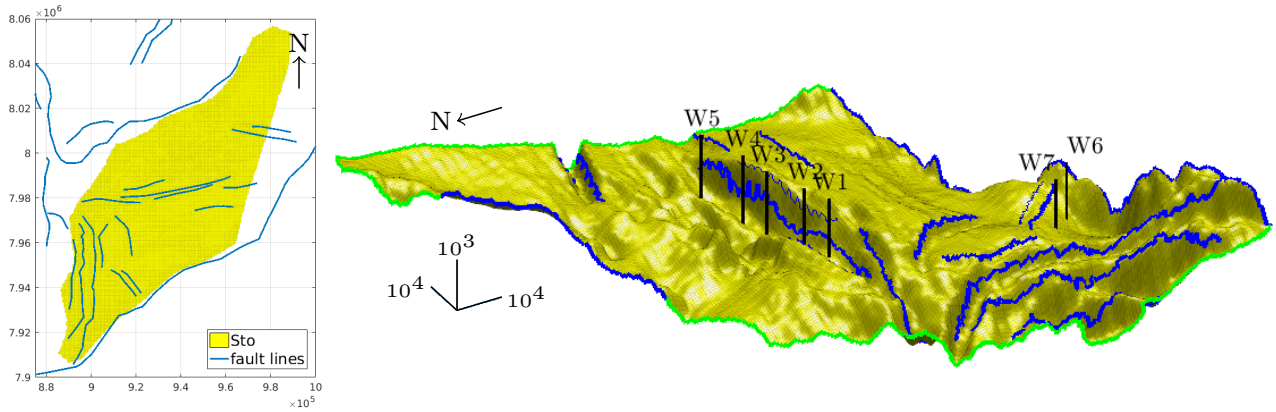


Figure 13: Faults in and surrounding the Stø aquifer (left), and implemented in the Stø geomodel (right). Coordinates in left plot are in ED50 UTM32, and scale in right plot is in meters. Colored edges in right plot: blue indicates fault faces, and green indicates open formation boundaries. Injection wells drawn in black with labels "W1", etc. Note that faults appear uneven on the figure as we are plotting the grid cell faces nearest to the continuous fault lines.

While our example illustrates the presence of sealing faults in an aquifer can limit the storage capacity, this is not always the case. Lothe et al. (2014) found the presence of sealing faults in a Norwegian aquifer (Garn) actually *increased* storage capacity while open faults lead to a lower capacity estimate. The reason their finding is different from ours is because their sealing faults acted to enhance the aquifer's structural trapping. In our example, sealing faults lead to high over-pressures which limited sustainable injection rates.

## 4. Concluding Remarks

To conclude, we have used two simplified methods to explore the impact that parameter uncertainty can have on $CO_2$ plume migration and storage capacity estimation. The parameters we focused on in the Utsira geomodel were porosity, permeability, caprock elevation, and aquifer conditions (pressure and temperature). We also considered the uncertainty of faults in the Stø geomodel, in terms of whether the fault is considered to be sealing, semi-sealing, or conducting (open). The purpose of this work was not to provide accurate storage capacities or plume behavior in the Utsira or Stø aquifers, rather, we wanted to illustrate the magnitude to which capacity estimates or plume dynamics can change in light of parameter variation due to uncertainty. We summarize a few of the interesting observations made in this work below.

First, we found that uncertainties in caprock elevation and permeability can have a greater impact on plume dynamics than uncertainties in porosity. Of course, the level of perturbations applied to these parameters controls the degree of impact on the system. However even after increasing the uncertainty range to $\approx \pm 50\%$ of the original average porosity, differences in plume migration were minimal; recall Table 1. On the other hand, the influence of porosity on plume migration was made clear for the idealized case in Figure 5; increasing the homogeneous porosity in the sloping aquifer by 30% noticeably reduced the speed of a migrating plume and its degree of upslope migration. Also evident in Figure 5 was the role that structural traps have in terms of containing $CO_2$ and effectively stabilizing the plume from migrating farther upslope and out of the domain.

Second, we found that average plume mismatch between the base Utsira model and a set of perturbed caprock surface models generally becomes worse over time as the plume continues to migrate; recall Figure 10. However, the plume mismatch for some of the perturbed surface models can actually improve over time, indicating the nonlinear behavior of the plume dynamics. Also, the trapping forecasts of an ensemble of highly perturbed caprock elevations in the southern part of Utsira revealed that the majority of the perturbed realizations had enough capacity to contain almost all the injected $CO_2$; recall Figure 11. This observation was due to the enhanced trapping capacity caused by high levels of caprock perturbation.

Third, we illustrated that variations in aquifer conditions can yield different structural storage capacity estimates; recall Figure 12. Pressure and temperature have a competing effect on $CO_2$ density and dictate whether it is found in its dense (i.e., liquid or supercritical) or non-dense (gaseous) form. For reasons related to storage efficiency, capacity estimates should be computed based on dense phase $CO_2$ amounts only.

Fourth, by simulating a range of injection rates in the faulted-geomodel for the Stø aquifer, we illustrated that the over-pressure induced when faults were treated as sealing limited the storage capacity more so than when faults were treated as open. While this may sound intuitive and has been shown to be the case for a sandstone basin in Birkholzer et al. (2011), we note that Lothe et al. (2014) found the presence of sealing faults in another Norwegian Continental Shelf formation could actually increase storage capacity due to more

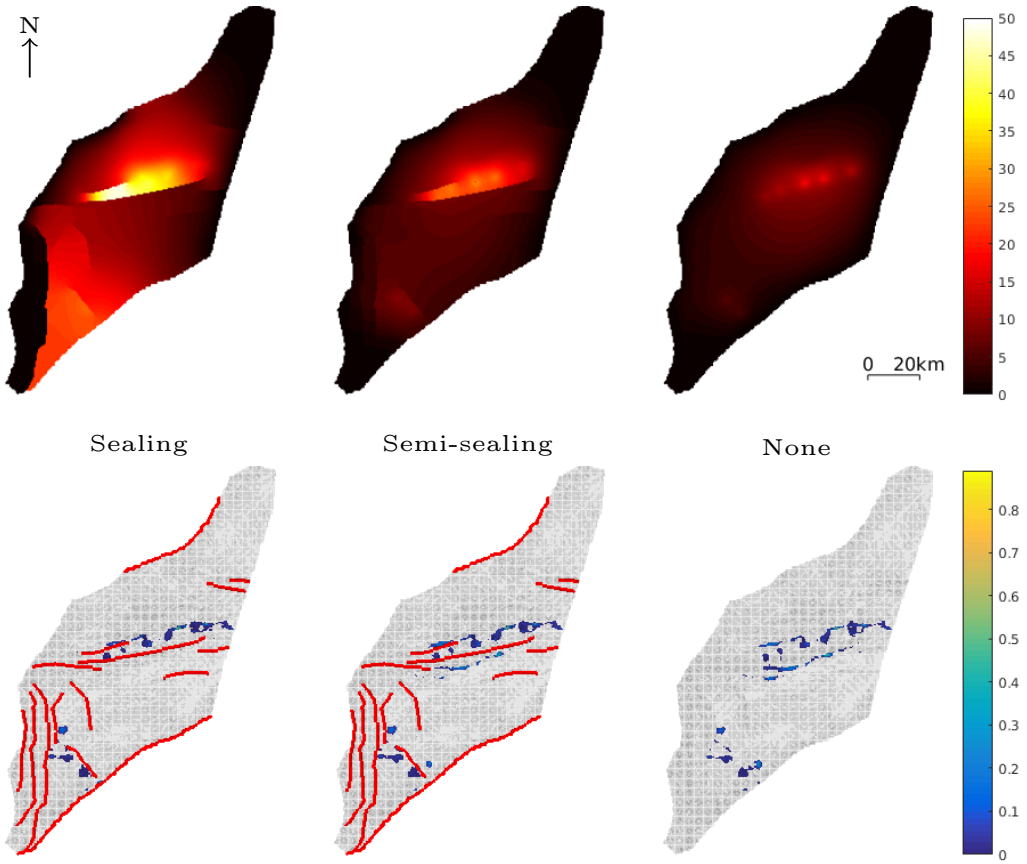


Figure 14: Comparison of fault case simulations given an injection rate of approximately 0.25 Mt/yr for each well. *Top row*: Over-pressure in bars at the year when the maximum over-pressure was reached. *Bottom row*: $CO_2$ saturation after 3000 years. (Saturation values range from 0 to 1 minus the residual saturation of water, and we have plotted all values above 0.01.) Faults are shown in red.

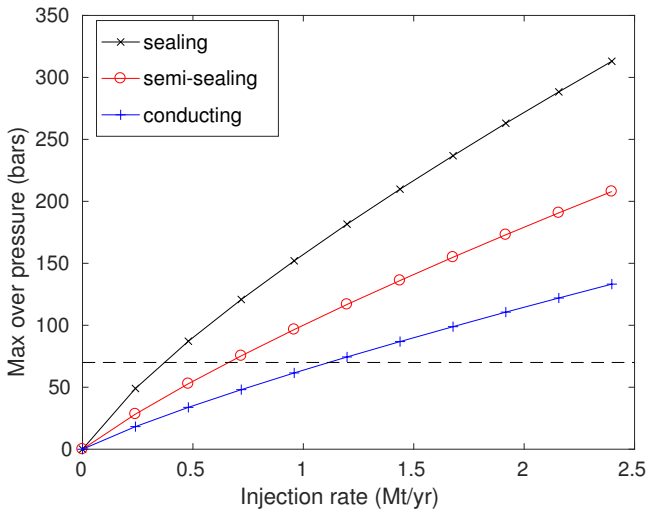


Figure 15: Impact of injection rate on maximum over-pressure simulated in three different fault cases. Dashed line indicates a hypothetical over-pressure limit.

structural trapping. As such, the final impact of faults on capacity is likely to be site specific. Similar to other geological heterogeneities, faults are a source of uncertainty in the geomodel, yet are easy to neglect in $CO_2$ storage modelling especially when data are scarce. However, since their influence on pressure buildup may limit sustainable injection rates, their presence and uncertainty ought to be represented in the geomodel.

A key component of this work was the use of rapid simulations and a reduction in the number of years to simulate, which was made possible through vertical-equilibrium modelling and a forecasting algorithm. We took the *one-factor-at-a-time* (*OFAT*) approach, in which the sensitivity of model responses to one parameter was evaluated at a time, and all other parameters where kept fixed to their base values. We recognize that this approach may not fully span the uncertainty space, and that it is rarely the case that a geomodel contains only one uncertain parameter. As such, future work should focus on cross-correlation effects of several geomodel parameters. Since this task would likely involve performing many more simulations than what were run in the present study, use of vertical-equilibrium modelling and migration forecasting in large-scale aquifers becomes even more valuable.

Whereas we simulated the injection and migration process for a fixed injection strategy only, future work could involve investigating the impact that parameter uncertainty has on plume migration in light of various injection scenarios (e.g., multiple injection sites, different injection schedules, etc.). Our analysis was focused primarily on plume migration and the trapping forecast. However, pressure buildup is also an important aspect of $CO_2$ storage, especially to ensure caprock integrity is not compromised by large-scale injection, and is deserving of future work.

## Acknowledgements

This work was funded in part by the Research Council of Norway through grant no. 243729 (Simulation and optimization of large-scale, aquifer-wide $CO_2$ injection in the North Sea).

## References

Allen, R., Nilsen, H. M., Andersen, O., Lie, K.-A., 2017. On obtaining optimal well rates and placement for $CO_2$ storage. Computational Geosciences 21 (5-6), 1403–1422.
10.1007/s10596-017-9631-6

Alnes, H., Eiken, O., Nooner, S., Sasagawa, G., Stenvold, T., Zumberge, M., 2011. Results from Sleipner gravity monitoring: Updated density and temperature distribution of the $CO_2$ plume. Energy Procedia 4, 5504–5511.
10.1016/j.egypro.2011.02.536

Ashraf, M., Lie, K.-A., Nilsen, H. M., Nordbotten, J. M., Skorstad, A., 2010. Impact of geological heterogeneity on early-stage $CO_2$ plume migration. In: Carrera, J. (Ed.), XVIII International Conference on Water Resources (CMWR). pp. 1–8.

Ashraf, M., Oladyshkin, S., Nowak, W., 2013. Geological storage of $CO_2$: Application, feasibility and efficiency of global sensitivity analysis and risk assessment using the arbitrary polynomial chaos. International Journal of Greenhouse Gas Control 19, 704–719.
10.1016/j.ijggc.2013.03.023

Bachu, S., 2003. Screening and ranking of sedimentary basins for sequestration of $CO_2$ in geological media in response to climate change. Environmental Geology 44 (3), 277–289.
10.1007/s00254-003-0762-9

Bachu, S., Bonijoly, D., Bradshaw, J., Burruss, R., Holloway, S., Christensen, N. P., Mathiassen, O. M., 2007. $CO_2$ storage capacity estimation: Methodology and gaps. International Journal of Greenhouse Gas Control 1 (4), 430–443.
10.1016/S1750-5836(07)00086-2

Bandilla, K. W., Celia, M. A., Janzen, A., Dobossy, M., Nordbotten, J. M., 2012. Applicability of vertical-equilibrium and sharp-interface assumptions in $CO_2$ sequestration modeling. International Journal of Greenhouse Gas Control 10, 134–147.
10.1016/j.ijggc.2012.04.015

Bandilla, K. W., Celia, M. A., Leister, E., 2014. Impact of model complexity on $CO_2$ plume modeling at Sleipner. Energy Procedia 63, 3405–3415.
10.1016/j.egypro.2014.11.369

Bear, J., Cheng, A. H.-D., 2010. Modeling groundwater flow and contaminant transport. Vol. 23. Springer Science & Business Media.

Birkholzer, J. T., Zhou, Q., Cortis, A., Finsterle, S., 2011. A sensitivity study on regional pressure buildup from large-scale $CO_2$ storage projects. Energy Procedia 4, 4371–4378.
10.1016/j.egypro.2011.02.389

Birkholzer, J. T., Zhou, Q., Tsang, C. F., 2009. Large-scale impact of $CO_2$ storage in deep saline aquifers: A sensitivity study on pressure response in stratified systems. International Journal of Greenhouse Gas Control 3 (2), 181–194.
10.1016/j.ijggc.2008.08.002

Cavanagh, A., Nazarian, B., 2014. A new and extended Sleipner benchmark model for $CO_2$ storage simulations in the Utsira formation. Energy Procedia 63, 2831–2835.
10.1016/j.egypro.2014.11.305

Cavanagh, A. J., Haszeldine, R. S., 2014. The Sleipner storage site: Capillary flow modeling of a layered $CO_2$ plume requires fractured shale barriers within the Utsira Formation. International Journal of Greenhouse Gas Control 21, 101–112.
10.1016/j.ijggc.2013.11.017

Cavanagh, A. J., Haszeldine, R. S., Nazarian, B., 2015. The Sleipner $CO_2$ storage site: using a basin model to understand reservoir simulations of plume dynamics. First Break 33 (June), 61–68.

Chadwick, A., Arts, R., Bernstone, C., May, F., Thibeau, S., Zweigel, P., 2008. Best practice for the storage of $CO_2$ in saline aquifers - observations and guidelines from the SACS and CO2STORE projects. In: British Geological Survey Occasional Publication. Vol. 14. Nottingham, UK, pp. 1–267, nora.nerc.ac.uk/2959/.

Cihan, A., Birkholzer, J., Bianchi, M., 2015. Optimal well placement and brine extraction for pressure management during $CO_2$ sequestration. International Journal of Greenhouse Gas Control 42, 175–187.
10.1016/j.egypro.2014.11.564

Coats, K., Dempsey, J., Henderson, J., et al., 1971. The use of vertical equilibrium in two-dimensional simulation of three-dimensional reservoir performance. Society of Petroleum Engineers Journal 11 (01), 63–71.

Dice, L. R., 1945. Measures of the Amount of Ecologic Association Between Species. Ecology 26 (3), 297–302.
10.2307/1932409

Espie, T., Woods, A., 2014. Testing some common concepts in $CO_2$ storage. Energy Procedia 63, 5450–5460.
http://dx.doi.org/10.1016/j.egypro.2014.11.576

Flett, M., Gurton, R., Weir, G., 2007. Heterogeneous saline formations for carbon dioxide disposal: Impact of varying heterogeneity on containment and trapping. Journal of Petroleum Science and Engineering 57 (1-2), 106–118.
10.1016/j.petrol.2006.08.016

Gasda, S. E., Nilsen, H. M., Dahle, H. K., 2013. Impact of structural heterogeneity on upscaled models for large-scale $CO_2$ migration and trapping in saline aquifers. Advances in Water Resources 62, 520–532.
10.1016/j.advwatres.2013.05.003

Gasda, S. E., Nilsen, H. M., Dahle, H. K., Gray, W. G., 2012. Effective models for $CO_2$ migration in geological systems with varying topography. Water Resources Research 48 (10), 1–17.
10.1029/2012WR012264

Gasda, S. E., Nordbotten, J. M., Celia, M. A., 2006. Significance of dipping angle on $CO_2$ plume migration in deep saline aquifers. In: Proceedings of the XVI International Conference on Computational Methods in Water Resources. No. June. pp. 18–22.

Gasda, S. E., Nordbotten, J. M., Celia, M. A., 2009. Vertical equilibrium with sub-scale analytical methods for geological $CO_2$ sequestration. Computational Geosciences 13 (4), 469–481.
10.1007/s10596-009-9138-x

Gasda, S. E., Wangen, M., Bjørnarå, T. I., Elenius, M. T., 2017. Investigation of Caprock Integrity Due to Pressure Build-up During High-volume Injection into the Utsira Formation. Energy Procedia 114, 3157–3166.
10.1016/j.egypro.2017.03.1444

Goater, A. L., Bijeljic, B., Blunt, M. J., 2013. Dipping open aquifers-The effect of top-surface topography and heterogeneity on $CO_2$ storage efficiency. International Journal of Greenhouse Gas Control 17, 318–331.
http://dx.doi.org/10.1016/j.ijggc.2013.04.015

Halland, E. K., Mujezinović, J., Riis, F. (Eds.), 2014. $CO_2$ Storage Atlas: Norwegian Continental Shelf. Norwegian Petroleum Directorate, npd.no/en/Publications/Reports/Compiled-CO2-atlas.

Han, W. S., Kim, K. Y., Esser, R. P., Park, E., McPherson, B. J., 2011. Sensitivity Study of Simulation Parameters Controlling $CO_2$ Trapping Mechanisms in Saline Formations. Transport in Porous Media 90 (3), 807–829.
10.1007/s11242-011-9817-7

Hesse, M. A., Orr, F. M., Tchelepi, H., 2008. Gravity currents with residual trapping. Journal of Fluid Mechanics 611, 35–60.
10.1017/S002211200800219X

Lie, K.-A., Nilsen, H. M., Andersen, O., Møyner, O., 2016. A simulation workflow for large-scale $CO_2$ storage in the Norwegian North Sea. Comput. Geosci. 20 (3), 607–622.
10.1007/s10596-015-9487-6

Lothe, A. E., Bergmo, P. E. S., Emmel, B. U., Mortensen, G. M., 2016. $CO_2$ Storage Capacity Estimates for a Norwegian and a Swedish Aquifer Using Different Approaches - From Theoretical Volumes, Basin Modelling to Reservoir Models. In: Vishal, V., Singh, T. N. (Eds.), Geological Carbon Sequestration. Springer International Publishing Switzerland, Ch. 6, pp. 97–117.
10.1007/978-3-319-27019-7_6

Lothe, A. E., Emmel, B., Grøver, A., Bergmo, P. E., 2014. $CO_2$ storage modelling and capacity estimation for the Trøndelag platform, offshore Norway - using a basin modelling approach. Energy Procedia 63, 3648–3657.
10.1016/j.egypro.2014.11.394

Lüth, S., Ivanova, A., Kempka, T., 2015. Conformity assessment of monitoring and simulation of $CO_2$ storage: A case study from the Ketzin pilot site. International Journal of Greenhouse Gas Control 42, 329–339.
10.1016/j.ijggc.2015.08.005

Manceau, J., Rohmer, J., 2016. Post-injection trapping of mobile $CO_2$ in deep aquifers: Assessing the importance of model and parameter uncertainties. Computational Geosciences 20 (6), 1251–1267.
10.1007/s10596-016-9588-x

Manceau, J. C., Rohmer, J., 2014. Ranking importance of uncertainties for the assessment of residual and dissolution trapping of $CO_2$ on a large-scale storage site. Energy Procedia 63, 3658–3664.
10.1016/j.egypro.2014.11.395

Martin, J. C., 1958. Some mathematical aspects of two phase flow with application to flooding and gravity segregation. Prod. Monthly 22 (6), 22–35.

Metz, B., Davidson, O., de Coninck, H., Loos, M., Meyer, L., 2005. IPCC 2005: IPCC Special Report on Carbon Dioxide Capture and Storage. Prepared by Working Group III of the Intergovernmental Panel on Climate Change. Cambridge University Press, United Kingdom and New York, NY, USA.

MRST, Dec. 2017b. The MATLAB Reservoir Simulation Toolbox. www.sintef.no/MRST.

MRST-co2lab, Dec. 2017b. Numerical $CO_2$ laboratory. www.sintef.no/co2lab.

Nilsen, H. M., Herrera, P. A., Ashraf, M., Ligaarden, I., Iding, M., Hermanrud, C., Lie, K.-A., Nordbotten, J. M., Dahle, H. K., Keilegavlen, E., 2011. Field-case simulation of $CO_2$-plume migration using vertical-equilibrium models. Energy Procedia 4, 3801–3808.
10.1016/j.egypro.2011.02.315

Nilsen, H. M., Krogstad, S., Andersen, O., Allen, R., Lie, K.-A., 2017. Using sensitivities and vertical-equilibrium models for parameter estimation of $CO_2$ injection models with application to Sleipner data. Energy Procedia.

Nilsen, H. M., Lie, K., Andersen, O., 2016a. Fully-implicit simulation of vertical-equilibrium models with hysteresis and capillary fringe. Computational Geosciences 20, 49–67.
10.1007/s10596-015-9547-y

Nilsen, H. M., Lie, K.-A., Andersen, O., 2015a. Analysis of $CO_2$ trapping capacities and long-term migration for geological formations in the Norwegian North Sea using MRST-co2lab. Computers and Geosciences 79, 15–26.
10.1016/j.cageo.2015.03.001

Nilsen, H. M., Lie, K.-A., Andersen, O., 2016b. Robust simulation of sharp-interface models for fast estimation of $CO_2$ trapping capacity. Computational Geosciences 20 (1), 93–113.
10.1007/s10596-015-9549-9

Nilsen, H. M., Lie, K.-A., Møyner, O., Andersen, O., 2015b. Spill-point analysis and structural trapping capacity in saline aquifers using MRST-co2lab. Computers & Geosciences 75, 33–43.
10.1016/j.cageo.2014.11.002

Nilsen, H. M., Syversveen, A. R., Lie, K.-A., Tveranger, J., Nordbotten, J. M., 2012. Impact of top-surface morphology on $CO_2$ storage capacity. International Journal of Greenhouse Gas Control 11, 221–235.
10.1016/j.ijggc.2012.08.012

Nordbotten, J. M., Celia, M. A., 2012. Geological Storage of $CO_2$: Modeling Approaches for Large-Scale Simulation. John Wiley & Sons, Inc.

Sarkarfarshi, M., Malekzadeh, F. A., Gracie, R., Dusseault, M. B., 2014. Parametric sensitivity analysis for $CO_2$ geosequestration. International Journal of Greenhouse Gas Control 23, 61–71.
10.1016/j.ijggc.2014.02.003

Shariatipour, S. M., Pickup, G. E., Mackay, E. J., 2016. Simulations of $CO_2$ storage in aquifer models with top surface morphology and transition zones. International Journal of Greenhouse Gas Control 54, 117–128.
10.1016/j.ijggc.2016.06.016

Singh, V., Cavanagh, A., Hansen, H., Nazarian, B., Iding, M., Ringrose, P., 2010. Reservoir Modeling of $CO_2$ Plume Behavior Calibrated Against Monitoring Data From Sleipner, Norway. In: SPE Annual Technical Conference and Exhibition. Florence, Italy.
10.2118/134891-MS

Sylta, Ø., 2004. Hydrocarbon migration modelling and exploration risk. Ph.D. thesis, Norwegian University of Science and Technology (NTNU), Trondheim, Norway.

Taku Ide, S., Jessen, K., Orr, F. M., 2007. Storage of $CO_2$ in saline aquifers: Effects of gravity, viscous, and capillary forces on amount and timing of trapping. International Journal of Greenhouse Gas Control 1 (4), 481–491.
10.1016/S1750-5836(07)00091-6

U.S. Department of Energy, Office of Fossil Energy, 2015. Carbon Storage Atlas. 5th Edition, netl.doe.gov/research/coal/carbon-storage/atlasv.

Zweigel, P., Arts, R., Lothe, A. E., Lindeberg, E. B. G., 2004. Reservoir geology of the Utsira Formation at the first industrial-scale underground $CO_2$ storage site (Sleipner area, North Sea). Geological Society, London, Special Publications 233 (1), 165–180.